Università degli Studi di Pisa

Corso di Laurea Magistrale in Fisica

Vlasov simulations of nonlinear wave dynamics and particle acceleration in laser-plasma interaction

Tesi di Laurea Magistrale

Candidato
Anna Grassi

Relatore
Dr. Andrea Macchi

Universita' di Pisa
Anno Accademico 2013/2014

Contents

Introduction

The study of completely ionized, high energy density plasmas generally requires a kinetic approach, because of the nonlinear dynamics of the particles interacting among themselves by means of the self-consistent electromagnetic force, and of the negligible role of collisions so that the plasma is far from an equilibrium condition.
The kinetic description starts with the definition of the distribution function $f(\vec{x}, \vec{p}, t)$, which represents the density of particles in an infinitesimal six-dimensional phase space volume $\mathrm{d}\vec{x} \cdot \mathrm{d}\vec{p}$, for each particle species. The fundamental equation that the distribution function has to satisfy is the Boltzmann equation. This is a transport equation, which describes the evolution of the distribution function due to the interaction among all the particles. In a dilute, hot plasma the interaction is dominated by the long-range forces due to the mean electromagnetic fields, rather than by binary interactions between the particles. For this reason, we can distinguish between the collective effects, due to the electromagnetic fields generated at a fixed position by all the particles, and the local collisional effects. The latter are negligible if $\nu_{coll} \ll \omega$, which means that the collision frequency is small in comparison with the characteristic frequency of variation of the fields. In collisionless plasmas, the Boltzmann equation describes the evolution of the distribution function in the phase space due to the external force and the self-consistent electromagnetic fields generated by the particles themselves. This is usually called Vlasov equation.
The intrinsic non linearity of the Vlasov equation, coupled with Maxwell's equations for the fields, allows to find an analytic solution in a very limited number of cases. Indeed, in 2010 Villani was awarded the Fields Medal for his work on this topic [1].
In order to overcome the difficulties of a theoretical description of the complex dynamics of plasmas in general and of laser-plasma interactions in particular, the use of a numerical approach is required, above all for an in-depth study of the involved collective effects.
Currently most of the plasma simulations are performed by PIC (Particle-in-Cell) codes (Lagrangian approach) [2], wherein the charged particles are modeled by macro-particles traced in the continuous phase space. This method solves a series of ordinary differential equations for the macro-particles motion on a space grid, and the Maxwell's equations for the fields.

Generally the PIC code requires a relative low computational effort, but on the other hand, because of the sampling of the distribution function, it prevents the study of low density regions of the phase space, and it is affected by an high level of statistical noise. Moreover, in the context of intense laser-plasma interaction, nonlinear and kinetic effects acquire remarkable importance, as these effects may generate non-thermal components of high energy particles.

For this reason, we have developed a so called *Vlasov code* (Eulerian approach), that performs a direct solution of the electromagnetic Vlasov equation on a phase space grid, coupled to the Maxwell's equations for the self-consistent electromagnetic fields. This method is a powerful tool for studying in details the particle dynamics due to the high resolution in the phase space. In our Vlasov code we made use of the canonical momentum conservation to obtain a reduced Vlasov equation in a 1D1P phase space while retaining the coupling with the laser pulse. For the numerical integration, a Time Splitting Scheme [3] and a flux conservative algorithm [4, 6] have been employed along with an original method to ensure exact mass conservation also in the relativistic regime. Violation of mass conservation was a known drawback of the use of splitting schemes for the 1D1P reduced scheme in the relativistic regime [7], for which quite complex methods have been previously proposed. Our method is much simpler than others, but apparently effective. Moreover, in order to evaluate the advantages and the drawbacks of the Vlasov approach, all the results have been compared with simulations performed with a 1D relativistic PIC code, in order to benchmark the results of the latter when changing the total number of particles used.

In this thesis we have developed the described numerical code for the application on two specific problems of current relevance in the framework of laser-plasma acceleration of electrons and ions, respectively.

The development in the last years of the laser technology opens the way for several research activities, mostly thanks to the CPA (Chirped Pulse Amplification) invention, which provides compact source of intense, high power, ultra short laser pulses. In the laser-plasma field the acceleration, of both electrons and ions, driven by superintense laser pulses is attracting an impressive attention, not only for the fundamental research but also for many potential applications. A plasma-based accelerator may overcome many of the fundamental limitation of the other accelerator structures, such as ionization or breakdown, and it should provide high-performance in a much smaller size. Novel regimes dominated by highly nonlinear dynamics can be achieved, due to the possibility to reach intensities up to $I \simeq 10^{21}$ W$\cdot cm^{-2}$.

Among the first mechanisms suggested in the field of laser-plasma electron acceleration, we focus on the one proposed by Tajima and Dawson in 1979, see Ref.[13], known as wakefield acceleration. Under certain conditions, as an intense laser pulse propagates in an underdense plasma, the ponderomotive force acting on the electron population generates plasma oscillations as wake waves behind the laser pulse itself. It was proven that the density oscillations

acquire a phase velocity equal to the group velocity of the laser pulse, so that the electrons moving with velocity close to the phase velocity of the waves can reach high energy by "surfing" on them. Thus the acceleration is not directly caused by the laser fields but it derives from the longitudinal electric field of the plasma waves.
If the wake wave is driven in the strongly nonlinear regime, close to its maximum amplitude, the so-called wavebreaking limit, a fraction of the electrons can overpass the wave itself and get trapped resonantly in the wave, allowing for their acceleration to high energy without the need for external injection. The first experimental evidence of electron acceleration by laser wakefield was given by [11]. Then high-quality bunches up to 100 MeV, and subsequently of the order of $\simeq$ 1GeV, have been produced by different research groups, as reported in Ref. [12] (and reference therein). Several analytic and numerical studies have been carried out within the assumption of cold plasma, exploiting the use of simulations for the investigation in the nonlinear regime [12]. Recently, see Ref.[19], Bulanov et al. directed their attention to the wavebreak process in a thermal plasma, in order to understand the role of the velocity distribution in the dynamics of the accelerated particles.
In this context, thanks to the use of the developed code, we can analyze the dynamics of the particles in the strongly relativistic regime so that, in the framework of an advanced particle acceleration scheme, our simulations may help to optimize the number and the spectrum of the electrons injected into the wake wave.
In addition, in the strongly nonlinear regime the density oscillation peaks composed by the accelerated electrons, may have an application as relativistic "flying mirror" for a counter propagating laser pulse, as first suggested in Ref.[20]. This seems to be a promising method for frequency upshift and focusing, as showed by Kando et al. in Ref.[23].
Concerning the laser-driven ion acceleration, several experiments have demonstrated the generation of multi-MeV proton beams in a wide range of laser and target parameters [34]. The production of high energy protons is due to different mechanisms that have been studied in order to allow the control of the main characteristics of the beam spectrum.
The interest on the possible applications is due to the most relevant feature of ions beam energy deposition in dense matter. Since the energy loss is dominated by Coulomb collisions, the cross section strongly grows with the decreasing of the energy, so that the process becomes progressively more efficient. Thus, differently from electrons and X-rays, an ion beam delivers most of its energy at the end of its path, at the so called Bragg peak. This property makes the protons and the ions very suitable for highly localized energy deposition. This is required for many applications, such as the use of protons as ignitor beam for Fast Ignition in the context of Inertial Confinement Fusion, radiobiological applications, medical hadrontherapy, and the production of Warm Dense Matter by isochoric heating of solid matter.
Among the various ion acceleration mechanisms, we focus on the so called *collisionless shock acceleration*. The acceleration is the consequence of the development of nonlinear electro-

static waves, in particular shock and soliton waves, excited by an intense laser interacting with an overdense plasma. This method is currently investigated as an advanced scheme for high energy ion generation, which are accelerated by reflection from the shock front.
In hydrodynamics a shock wave is a discontinuous solution of the ideal fluid equations which propagates with velocity greater than the sound speed, and involves an abrupt change in the macroscopic plasma state that is mediated by collisional effects. In principle, the formation of a collisionless electrostatic shock solution is not possible within the fluid description, where only soliton solutions appear as the result of a balance between dispersion and nonlinearity that causes the wave to steepen. A shock wave solution becomes possible in the presence of kinetic effects acting as an effective dissipation which breaks the symmetry of the soliton. For instance, assuming a fraction of the ions population to be reflected at the shock front by the electrostatic potential, a shock solution may be found, as explained in Ref.[32]. This also shows that the ion acceleration associated to a collisionless shock may be inherent to the shock formation rather than a consequence of it.
A recent experiment, see [29], has reported a relevant result in this context. Hederberger et al. using a CO_2 laser pulse, have observed protons up to ~ 20 MeV, with an energy spread $\sim 1\%$, in a laser-produced hydrogen plasma. They have attributed the narrow monoenergetic peaks observed in the ion energy spectrum to the generation of a collisionless shock driven by the laser-heated electrons. Moreover, several numerical studies [26, 27, 28] have investigated on the main features either of the soliton or the shock solutions and the related acceleration. The studies concerning shock waves are of remarkable importance also for astrophysical and space plasmas, for example in order to explain acceleration of cosmic-ray particles. Moreover, the frontier laboratory experiments may emulate the conditions of the astrophysical phenomena, or at least give a reproduction by a scaling of each physical quantity, with the state-of-the-art laser system [25].
In the first part of this thesis we present (Chapter 2) the numerical methods we have used and, in particular, we give a detailed description of the developed Vlasov code. In Chapter 3 we address the problem of laser wakefield acceleration. In the first part we provide a description of the acceleration mechanism for cold and thermal plasmas, then we discuss our results on the relativistic electron dynamics. The analysis on soliton and shock waves is presented in Chapter 4, starting with a description of the phenomena that lead to the generation of these nonlinear waves. In the second part of the Chapter we focus on our simulation and analytic results. Then, we summarize the presented original results and we give specific suggestions for the future development of the work.

Chapter 1

Numerical Methods

1.1 Introduction

Recent increase in power and memory of supercomputers enable simulations to become more and more useful for the study of complex systems with unprecedented resolution. A numerical approach is used in almost all the areas of plasma physics, such as fusion energy research, plasma accelerators, space physics, and many others.
The interest on the study of resonant wave-particles interactions and above all, on the large number of phenomena with essential kinetic nature, entails the necessity to use fully kinetic equations and furthermore numerical simulations. The basis for a kinetic description of the plasma dynamics is the Boltzmann equation for $f_\alpha(\vec{x},\vec{p},t)$, the distribution function of the α-th species,

$$\partial_t f_\alpha + \frac{\vec{p}}{m\gamma}\cdot\vec{\nabla}_x f_\alpha + \vec{F}_\alpha\vec{\nabla}_p f_\alpha = (\partial_t f_\alpha)_{coll} \tag{1.1}$$

where the force $\vec{F}_\alpha = q_\alpha(\vec{E} + \frac{\vec{v}}{c}\times\vec{B})$ is the Lorentz force acting on a particle, due to the electromagnetic field that satisfies Maxwell's equations :

$$\begin{cases}\vec{\nabla}\cdot\vec{B} = 0\\ \vec{\nabla}\times\vec{E} = -\frac{1}{c}\partial_t\vec{B}\end{cases}\qquad\qquad\begin{cases}\vec{\nabla}\cdot\vec{E} = 4\pi\rho\\ \vec{\nabla}\times\vec{B} = \frac{1}{c}\partial_t\vec{E} + \frac{4\pi}{c}\vec{J}\end{cases} \tag{1.2}$$

The source terms depend on the motion of the particles constituting the plasma itself and are computed from the distribution function as

$$\begin{aligned}\rho(\vec{x},t) &= \textstyle\sum_\alpha q_\alpha \int f_\alpha(\vec{x},\vec{p}_\alpha,t)\mathrm{d}\vec{p}_\alpha\\ \vec{J}(\vec{x},t) &= \textstyle\sum_\alpha q_\alpha \int \frac{\vec{p}_\alpha}{m_\alpha\gamma_\alpha}\cdot f_\alpha(\vec{x},\vec{p}_\alpha,t)\mathrm{d}\vec{p}_\alpha\end{aligned} \tag{1.3}$$

where we have used $\gamma_\alpha = \sqrt{1 + \frac{|\vec{p}_\alpha|^2}{m_\alpha^2 c^2}}$.
So we obtain a non-linear system that represents the evolution of the distribution function by the action of self-consistent electromagnetic fields.
In this thesis, we focus on collisionless fully ionized plasmas, so we take for each species in eq.(1.1) the collisional term $(\partial_t f_\alpha)_{coll} = 0$.

In the following we present two different kinetic methods: the Particle-In-Cell method (Lagrangian approach) wherein charged particles are modeled by macro-particles traced in the continuous phase space, and the Vlasov method (Eulerian approach), which provides a direct integration of Vlasov equation on a phase space grid.

1.2 Particle-In-Cell method

Historically, simulations of collisionless plasma system have been carried out mostly by PIC (Particle-In-Cell) codes. The basic idea of this method is to simulate the plasma system by following the trajectories of particles in a continuous phase space, and to compute moments of the distribution function, such as the density and current on an Eulerian grid.
This yields a great simplification: instead of finding the solution of the Vlasov partial differential equation, the code solves a series of ordinary differential equations for the motion of charged particles, with self-consistent fields calculated by integration of the Maxwell's equations.
Numerically there is no possibility to take into account all the particles of a plasma. It is necessary to employ a statistical approach, whereby we give a discrete representation of the continuous distribution function, regarding the 1D case

$$f(q,p,t) = f_0 \sum_{n=0}^{N_p-1} g[q - q_n(t)]\delta[p - p_n(t)] \tag{1.4}$$

where f_0 is the normalization constant, q represents the spatial coordinate, p is the conjugated momentum variable, and $q_n(t), p_n(t)$ denote the trajectory in phase space of the n-th particle. Thus, in the simulation the trajectories of the particles are solved for all the computational particles, whereas the number of real particles would be much greater than N_p.
Limiting our presentation to the one dimensional case, the distribution function in eq.(1.4) assigns to each computational particle distribution a specific functional form, given by the product of the shape in each direction of the phase space. Thus, we opt for a Dirac's delta function shape in the momentum space and for an extended shape in the real space, defined by the function $g(x)$, centered over the average position $q_n(t)$. We assume $f(q,p,t)$ defined

as in Eq.(1.4) to be a solution of the Vlasov equation that from Eq.(1.1) becomes

$$\partial_t f + \frac{p}{m\gamma}\partial_q f + F\partial_p f = 0 \tag{1.5}$$

Substituting eq.(1.4) in eq.(1.5), the three terms become

$$\begin{gathered}
\partial_t f = -f_0 \textstyle\sum_n \{\dot{q}_n(t)\partial_q g[q-q_n(t)]\delta[p-p_n(t)] + g[q-q_n(t)]\dot{p}_n(t)\partial_p\delta[p-p_n(t)]\} \\
\tfrac{p}{m\gamma}\partial_q f = f_0 \textstyle\sum_n \{\tfrac{p_n(t)}{m\gamma_n}\partial_q g[q-q_n(t)]\delta[p-p_n(t)]\} \\
F\partial_p f = f_0 \textstyle\sum_n \{F[q,p_n(t),t]g[q-q_n(t)]\partial_p\delta[p-p_n(t)]\}
\end{gathered} \tag{1.6}$$

By summing these and integrating over dp and over dq respectively, we have

$$\begin{gathered}
\textstyle\sum_n(-\dot{q}_n(t) + \tfrac{p_n}{m\gamma_n})\partial_q g[q-q_n(t)] = 0 \\
\textstyle\sum_n(-\dot{p}_n(t) + \bar{F}_n)\partial_p\delta[p-p_n(t)] = 0
\end{gathered} \tag{1.7}$$

Since these relations have to be fulfilled for every possibly choice of the shape function, we obtain

$$\dot{q}_n = \frac{p_n}{m\gamma_n} \quad ; \quad \dot{p}_n = \bar{F}_n \tag{1.8}$$

With $\bar{F}_n(q_n,p_n,t) = \int g(q-q_n)F(q,p_n,t)\mathrm{d}q$ we denote the spatial average of the Lorentz force on the n-th particle. This means that each computational particle follows the same phase space trajectory that a single particle would do.
We obtain eq.(1.8) by supposing for the function g the same properties as the delta function

$$\int g(q-q_n)\mathrm{d}q \quad = \quad 1 \quad ; \quad \int \partial_q g(q-q_n)\mathrm{d}q = 0 \tag{1.9}$$

Thanks to this assumption the normalization constant becomes $f_0 = \frac{1}{N_p}$.
So, we switched to a Lagrangian description and we proved that the problem of solving the kinetic equation for the distribution function $f(q,p,t)$ can be reduced to a system of $2N_p$ ordinary differential equations.
The number of such macro-particles must be chosen high enough to collect a sufficient statistics on the particle motion. Indeed, because of the sampling of the distribution function, the fundamental weakness of PIC codes is the high level of statistical noise that can be reduced by increasing the number of computational particles. However the decreasing of the fluctuation is not very fast due to the dependence of the statistical noise on $\propto \frac{1}{\sqrt{N_p}}$.
A large value of N_p is also necessary in order to properly resolve low density values. Indeed,

we can estimate the smallest density variation we account of as $\delta n \simeq \frac{n_0}{N_p}$, with n_0 initial density in the cell. Thus, the use of many particles per cell is essential to limit the statistical noise and to make possible the study of low density regions of the phase space. Despite that, the increasing number of particles corresponds to a greater request of available memory and a bigger computational effort. For this reason we should find a good compromise in the choice of this parameter before starting the simulation.

We now explain how the code performs a complete cycle over a discretized temporal step Δt.

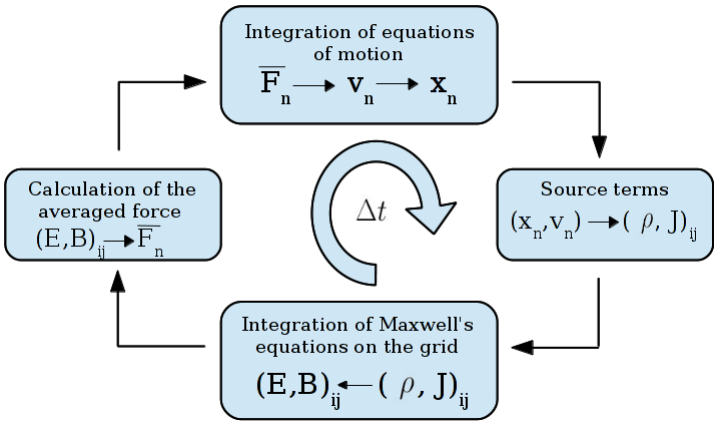

Figure 1.1: Time-cycle of the PIC method.

The loop shown in Fig.(1.1) is repeated iteratively for the fixed number of time steps. As we can see, once the force is computed, the new momenta and the positions of the particles can be calculated. At this point, we can update the densities and the currents, and then compute again the fields needed for advancing the Lorentz force.
In the literature, the algorithms more commonly mentioned for the integration of the equations of motion are the so called leap-frog scheme in order to advance the positions and the Boris-pusher for the momenta. These algorithms are also implemented in the code we use.
The leap-frog scheme represented in Fig.(1.2) allows us to advance the position of a particle from time step t^n to t^{n+1}, using the velocity calculated at the mid-point of a time step $t^{n+\frac{1}{2}}$.

$$x(t^{n+1}) = x(t^n) + \Delta t \cdot v(t^{n+\frac{1}{2}}) \tag{1.10}$$

Note that the leap-frog algorithm is second order accurate. For an explanation of the Boris-pusher we refer to [2].
In order to calculate the Lorentz force using fields which are self-consistents with particle dy-

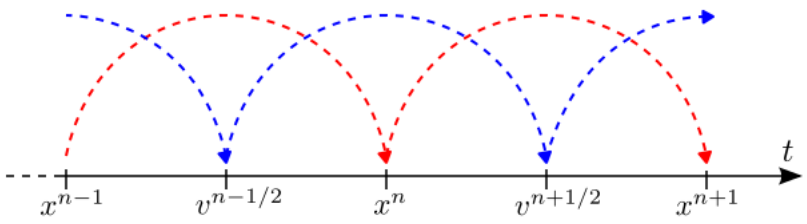

Figure 1.2: Leap-frog scheme

namics, we need to determine the source terms to be introduced in Maxwell's equations. The charge and current density can be obtained as in eq.(1.3) as the integral over the momentum variable of the distribution function defined in eq.(1.4), and summing over the species index α, we get

$$\begin{aligned} \rho(x,t) &= f_0 \textstyle\sum_{\alpha,n} q_\alpha g[x - x_n(t)] \\ \vec{J}(x,t) &= f_0 \textstyle\sum_{\alpha,n} q_\alpha \vec{v}_n g[x - x_n(t)] \end{aligned} \tag{1.11}$$

with $\vec{v}_n = \frac{\vec{p}_n}{m\gamma_n} = \frac{\vec{p}_n}{\sqrt{m^2 + \frac{|\vec{p}_n|^2}{c^2}}}$.

First of all, the algorithm for the integration of fields requires to define a fixed mesh in real space where to project particles positions, in order to interpolate charge and current density. Thus in the following we take into account an Eulerian grid with x_i center of i-th cell, Δx cell extension, and $x_{i+\frac{1}{2}}$ right boundary.

Therefore at a given time step, all the macro-particles whose center position is situated in the i-th cell $x_{i-\frac{1}{2}} < x_n < x_{i+\frac{1}{2}}$, contribute to the density and current of that cell, and its neighbors. In detail, in the PIC code used, the shape of the density distribution associated with each particle is defined as

$$g(x) = \begin{cases} 1 + \frac{x}{\Delta x} & \text{if} \quad -\Delta x < x < 0 \\ 1 - \frac{x}{\Delta x} & \text{if} \quad 0 < x < \Delta x \\ 0 & \text{if} \quad |x| > \Delta x \end{cases} \tag{1.12}$$

With this choice, each particle lies over three cells, the one where the center position is situated and the adjacent cells on the right and on the left. Summing the contribute of all the particles for each cell, it is possible to find the density explicitly.

The set of equations above, provides a closed description once we chose an algorithm to solve Maxwell's equations.

1.3 Vlasov method

Vlasov codes represent a tool alternative to PIC method for studies of collisionless plasmas. Especially if we are interested in fine resolution of the phase space, including regions with very low values of the distribution function, Vlasov codes could be necessary for understanding physical phenomena.
Currently most of the plasma simulations are performed by PIC codes, which solve ordinary differential equations of macro-particle motion with a relatively low numerical effort.
As said before, the main drawback of PIC codes arises with the corse-graining of the continuous distribution function, because it introduces a large amount of statistical noise. Moreover the use of a limited number of macro-particles involves a minimum value of the density that can be accurately resolved. This may prevent us investigating about high energy particle acceleration, particle trapping, and so on.
Instead, Vlasov codes guarantee us the same accuracy over all the phase space and a very fine resolution. The price for this useful property is the greater numerical complexity and the longer time required for simulations, above all for two and three dimensional systems.

The aim of this paragraph is to show how to compute a solution of the relativistic 1D Vlasov equation along the x-axis

$$\frac{\partial f}{\partial t} + \frac{p_x}{M\gamma} \cdot \frac{\partial f}{\partial x} + q\left(\vec{E} + \frac{\vec{p}}{M\gamma} \times \vec{B}\right) \frac{\partial f}{\partial \vec{p}} = 0 \tag{1.13}$$

Generally, the distribution function depends on the three component of the momentum, as $f = f(x, \vec{p}, t)$. We show how to reduce the problem to an 1D1V geometry exploiting the conservation of transverse canonical momentum defined in Eq.(1.14), where $\vec{A}_\perp$ denotes the transverse component of the vector potential.

$$\vec{\Pi}_\perp = \vec{p}_\perp + q \cdot \vec{A}_\perp \tag{1.14}$$

We are allowed to use this conservation because we take into account non-magnetized plasmas, i.e. the longitudinal magnetic field component along the x-axis vanishes. Therefore, if we regard the Hamiltonian of a single particle in the electromagnetic field, expressing the momentum $\vec{p}$ in terms of the vector potential $\vec{A}$ and of the canonical momentum $\vec{\Pi}$, we obtain

$$H = Mc^2 \left(1 + \frac{(\vec{\Pi} - q\vec{A})^2}{M^2c^2}\right)^{\frac{1}{2}} + q\phi(x,t) \tag{1.15}$$

where $\phi(x,t)$ is the electrostatic potential. From the Hamiltonian equation $\frac{\mathrm{d}\vec{\Pi}}{\mathrm{d}t} = -\frac{\partial H}{\partial \vec{x}}$, we

obtain that the transverse canonical momentum fulfills Eq.(1.16) and it is conserved.

$$\frac{\mathrm{d}\vec{\Pi}_\perp}{\mathrm{d}t} = -\vec{\nabla}_\perp H = 0 \tag{1.16}$$

Moreover, without loss of generality we can set $\vec{\Pi}_\perp(x, t = 0) = \vec{\Pi}_\perp(x, t) = 0$ obtaining the following Hamiltonian

$$H = Mc^2 \left(1 + \frac{p_x^2}{M^2c^2} + \frac{q^2 \mid \vec{A}_\perp \mid^2}{M^2c^2}\right)^{\frac{1}{2}} + q\phi(x, t) \tag{1.17}$$

The corresponding Vlasov equation can be written in the form

$$\frac{\partial f}{\partial t} + \frac{\partial H}{\partial p_x} \cdot \frac{\partial f}{\partial x} - \frac{\partial H}{\partial x} \cdot \frac{\partial f}{\partial p_x} = 0 \tag{1.18}$$

inserting Eq.(1.17) in Eq.(1.18), we get

$$\frac{\partial f}{\partial t} + \frac{p_x}{M\gamma} \cdot \frac{\partial f}{\partial x} + q\left(E_x - \frac{q}{2M\gamma}\frac{\partial \mid \vec{A}_\perp(x,t) \mid^2}{\partial x}\right)\frac{\partial f}{\partial p_x} = 0 \tag{1.19}$$

This means that we can seek a solution for a distribution function only depending on x and p_x variables.
It is clear from the previous equation that the problem is reduced to the 1D1V case, thus the eq.(1.13) becomes

$$\frac{\partial f}{\partial t} + \frac{p_x}{M\gamma} \cdot \frac{\partial f}{\partial x} + q\left(E_x + (\frac{\vec{p}}{M\gamma} \times \vec{B})_x\right)\frac{\partial f}{\partial p_x} = 0 \tag{1.20}$$

This equation has to be coupled with Maxwell's equations for self-consistent fields, generated by charge densities and currents of plasma particles. The latter quantities are defined in eq.(1.3) and are calculated over all the grid cells.
So first of all, we chose a fixed mesh in x and p_x direction. The dimension of the grid can be changed for different problems we have to deal with, and the same for the dimension of the cell, in order to properly resolve the shortest length scale of phenomena we are interested in.

Now we can start explaining the methods used in the code, the Time Splitting Scheme and the Flux Balance Method.

1.3.1 Time Splitting Scheme and Flux Balance Method

The Time Splitting Scheme (TSS) procedure was used for the first time by Cheng and Knorr [3]. The integration of eq.(1.20) can be performed numerically splitting the Vlasov equation in two partial derivative transport type equations.
After splitting, the solution of each equation can be obtained by several methods. We have implemented the Positive and Flux Conservative Method based on Flux Balance Method (FBM) [4, 5].
The latter appears to be the most suitable for parallelization purposes and it works well with our choice of boundary conditions.

In order to simplify the explanation of the TTS and FBM, we present the 1D electrostatic case, in which the Vlasov equation has the form

$$\frac{\partial f}{\partial t} + v_x \frac{\partial f}{\partial x} + \frac{qE_x}{m}\frac{\partial f}{\partial v_x} \quad = \quad 0 \tag{1.21}$$

and it is coupled with Poisson's equation. Acting the splitting, it reduces to the following couple of equations:

$$\begin{cases} \frac{\partial f_1}{\partial t} + v_x \frac{\partial f_1}{\partial x} = 0 \\ \\ \frac{\partial f_2}{\partial t} + \frac{qE_x}{m}\frac{\partial f_2}{\partial v_x} = 0 \end{cases} \tag{1.22}$$

The formal solution should be

$$f_1(x, v_x, \Delta t) \quad = \quad f_1(x - v_x \Delta t, v_x, 0) \quad , \quad f_2(x, v_x, \Delta t) = f_2(x, v_x - \frac{qE_x(\bar{x}, \bar{t})}{m_e}\Delta t, 0) \tag{1.23}$$

with $0 < \bar{t} < \Delta t$, $x - v_x \Delta t < \bar{x} < x$. It represents a shift in the x-axis and one in the v_x-axis, considering the electric field to be known from the Poisson's equation.
In order to obtain a second order symmetrical scheme from the time step t^n to t^{n+1}, it is necessary to :

1. Evolve the first equation for $\frac{\Delta t}{2}$ $\longrightarrow f^*(x, v_x) = f^n(x - v_x \frac{\Delta t}{2}, v_x)$
2. Evolve the second equation for Δt $\longrightarrow f^{**}(x, v_x) = f^*(x, v_x - \frac{qE_x(x)}{m_e}\Delta t)$
3. Evolve the first equation for $\frac{\Delta t}{2}$ $\longrightarrow f^{n+1}(x, v_x) = f^{**}(x - v_x \frac{\Delta t}{2}, v_x)$

Substituting the result of step 1 and 2 in f^{n+1} we get

$$f^{n+1}(x, v_x) = f^n(x - \Delta t(v_x - \frac{qE_x(\bar{x})}{2m_e}\Delta t),\ v_x - \frac{qE_x(\bar{x})}{m_e}\Delta t) \tag{1.24}$$

where $E_x(\bar{x}) = E_x(x - v_x\frac{\Delta t}{2},\, t + \frac{\Delta t}{2})$. Since the shift in the velocity space does not change the density, the fields can be updated after the solution of step 1, i.e. at half time step as required for a leap frog scheme. As the solution for the longitudinal electric field is correct to the first order, we have found a complete solution that is correct up to the second order. Explicitly, in the code the solution of the first of Eq.(1.22) is used as an initial condition for the second one, and vice versa. Moreover, in order to save in each iteration the calculation of a shift along x-direction, we can connect the two consecutive half time step shift (step 3 and step 1) in one single time step shift.

Let's show how FBM can be used to obtain a numerical solution of a general equation as

$$\frac{\partial f}{\partial t} + \frac{\partial}{\partial x}(af(x,t)) = 0 \tag{1.25}$$

This equation has exactly the same structure of eq.(1.22) since $\frac{\partial a}{\partial x} = \frac{\partial v_x}{\partial x} = 0$ and $\frac{\partial a}{\partial x} = \frac{\partial E_x}{\partial v_x} = 0$. So we are going to solve eq.(1.25) and then return to the solution of the system of equations (1.22) recalling the needed substitutions :

$$\begin{cases} a \to v_x \\ x \to x \end{cases} \quad ; \quad \begin{cases} a \to \frac{qE_x}{m} \\ x \to v_x \end{cases} \tag{1.26}$$

Considering the distribution function smooth enough in each cell, we can define the mean quantity

$$\overline{f(x,t)} = \frac{1}{\Delta x} \int_{-\frac{\Delta x}{2}}^{+\frac{\Delta x}{2}} f(x+h,t)\mathrm{dh} \tag{1.27}$$

that fulfills the same equation as $f(x,t)$. If we insert $\overline{f(x,t)}$ in Eq.(1.25), it becomes

$$\partial_t \overline{f(x,t)} + \frac{1}{\Delta x}[af(x + \frac{\Delta x}{2}, t) - af(x - \frac{\Delta x}{2}, t)] = 0 \tag{1.28}$$

and integrating over a time step

$$\overline{f(x,t+\Delta t)} = \overline{f(x,t)} - \frac{1}{\Delta x} \int_{t}^{t+\Delta t} [af(x + \frac{\Delta x}{2}, t) - af(x - \frac{\Delta x}{2}, t)]\mathrm{dt} \tag{1.29}$$

If we consider $x = x_i$ the i-th cell in our mesh and Δx the extension of the cell, in the previous integral we recognize the quantity of flux of distribution function lost or gained at the cell boundary. Indeed the integral sums the quantity of distribution function that reaches the boundary during an interval Δt.

In order to define these fluxes in detail, we can assume that what arrives at the boundary has to be contained at the initial time t in the range $(x_i + \frac{\Delta x}{2} - a\Delta t\ ,\ x_i + \frac{\Delta x}{2})$.
If we substitute the function $h(t) = x_i + \frac{\Delta x}{2} - a \cdot t$, with $\mathrm{d}h = -a \cdot \mathrm{d}t$ into Eq.(1.29) we get

$$\overline{f(x_i, t+\Delta t)} = \overline{f(x_i, t)} - \frac{1}{\Delta x}\left[\int_{x_i+\frac{\Delta x}{2}-a\Delta t}^{x_i+\frac{\Delta x}{2}} f(h,t)\mathrm{dh} - \int_{x_{i-1}+\frac{\Delta x}{2}-a\Delta t}^{x_{i-1}+\frac{\Delta x}{2}} f(h,t)\mathrm{dh}\right] \tag{1.30}$$

The first integral represents the flux of distribution function lost by the cell x_i at its right boundary in case of $a > 0$, or gained if $a < 0$, because the integration runs over the initial position of the distribution function that after a time step will reach the right boundary, and the right boundary itself.
At this point it is necessary to approximate $f(x,t)$ in order to be able to calculate the integral and thus to have a reconstruction of the distribution function on each grid cell.
First, we present a reconstruction by linear function approximation as

$$f(x,t) = f(x_i) + (f(x_{i+1}) - f(x_{i-1})) \cdot \frac{x}{2\Delta x} \tag{1.31}$$

with $x_i - \frac{\Delta x}{2} < x < x_i + \frac{\Delta x}{2}$. Note that we have to ensure that the function $h(t)$ does not go out of the i-th cell, that means $a\Delta t < \Delta x$. Recalling eq.(1.26), this request forces our choice of simulation parameters so that

$$\frac{\Delta x}{\Delta t} > v_x \quad ; \quad \frac{\Delta v_x}{\Delta t} > \frac{qE}{m} \tag{1.32}$$

These relations also correspond to the well known Courant's conditions [2]. These are necessary conditions for the stability of the numerical solution of partial differential equations.
As an example we can calculate explicitly the first flux integral for positive a :

$$\Phi_i = \frac{1}{\Delta x}\int_{x_i+\frac{\Delta x}{2}-a\Delta t}^{x_i+\frac{\Delta x}{2}} f(h,t)\mathrm{dh} =$$

$$= f(x_i,t)\cdot a\frac{\Delta t}{\Delta x} + (f(x_{i+1},t) - f(x_{i-1},t))\cdot a\frac{\Delta t}{4\Delta x}\left(1 - a\frac{\Delta t}{\Delta x}\right) \tag{1.33}$$

If $a < 0$ the flux is $\Phi_i = f(x_i,t)|a|\frac{\Delta t}{\Delta x} - (f(x_{i+1},t) - f(x_{i-1},t))|a|\frac{\Delta t}{4\Delta x}(1 - |a|\frac{\Delta t}{\Delta x})$, and the complete solution is :

$$\begin{cases} f(x_i, t+\Delta t) = f(x_i,t) + \Phi_{i-1} - \Phi_i & \text{for } a > 0 \\ f(x_i, t+\Delta t) = f(x_i,t) + \Phi_{i+1} - \Phi_i & \text{for } a < 0 \end{cases} \tag{1.34}$$

Using a linear interpolation the positivity of $f(x,t)$ is not preserved, so we implement the third order approximation method explained in the next paragraph.

1.3.2 Positive and Flux Conservative Method

The method implemented to solve the system (1.22) is the Positive and Flux Conservative Method based on the Flux Balance Method [4, **?**]. The main advantage we achieve using it is the conservation of the positivity of the distribution function in each grid point. Moreover, it enables us to control spurious oscillations that may arise in long time simulations due to negative value of $f(x,p_x,t)$, and it conserves total particle mass.

Starting from eq.(1.30) the method provides for a reconstruction via a primitive function, defined by

$$F(x_i+\frac{\Delta x}{2},t)-F(x_i-\frac{\Delta x}{2},t) \quad = \int_{x_i-\frac{\Delta x}{2}}^{x_i+\frac{\Delta x}{2}} f(x,t)\mathrm{d}x = \Delta x\cdot\overline{f(x_i,t)} \tag{1.35}$$

and so $F(x_i+\frac{\Delta x}{2},t)=\Delta x\sum_{k=0}^{i}\overline{f(x_k,t)}$.
Giving an approximation of $F(x,t)$ of the second order in the interval $[x_{i-\frac{1}{2}},x_{i+\frac{1}{2}}]$ we get

$$F(x,t)=\Delta x\sum_{k=0}^{i-1}\overline{f(x_k,t)}+(x-x_{i-\frac{1}{2}})\overline{f(x_i,t)}+\frac{1}{2}(x-x_{i-\frac{1}{2}})(x-x_{i+\frac{1}{2}})\frac{\overline{f(x_{i+1},t)}-\overline{f(x_i,t)}}{\Delta x} \tag{1.36}$$

from this we obtain by differentiation

$$f(x,t)=\frac{dF(x,t)}{dx}=\overline{f(x_i,t)}+(x-x_i)\frac{\overline{f(x_{i+1},t)}-\overline{f(x_i,t)}}{\Delta x} \tag{1.37}$$

We obtain also the flux as the value of the primitive function calculated at the integration limits of eq.(1.30).
In the same way, we can accomplish a third order approximation. Since we are looking for a positive scheme, we need to introduce slope correctors so that steep gradients are avoided. Considering the case in which between two adjacent cells there is a big difference in the value of the distribution function. It is possible that the flux outgoing from the i-th cell, calculated as (1.33) or as the same integral with the distribution function defined in (1.37), results bigger than the value of the distribution function in the same cell. This produces a remaining distribution function in the i-th cell with negative value.

For this reason we use the slope correctors defined as

$$\varepsilon_i^+ \begin{cases} \min(1; 2\frac{f_i}{f_{i+1}-f_i}\ ) & \text{if } f_{i+1}-f_i > 0, \\ \min(1; -2\frac{f_\infty - f_i}{f_{i+1}-f_i}) & \text{if } f_{i+1}-f_i < 0, \end{cases} \quad \varepsilon_i^- \begin{cases} \min(1; 2\frac{f_\infty - f_i}{f_i - f_{i-1}}) & \text{if } f_i - f_{i-1} > 0, \\ \min(1; -2\frac{f_i}{f_i - f_{i-1}}) & \text{if } f_i - f_{i-1} < 0, \end{cases} \tag{1.38}$$

with $f_\infty = \max_{j\in I}\{f_j\}$ maximum value over all the mesh.
Thus the allowed greatest variation between two neighbor cells is three times the value of the distribution function in the first cell. For larger differences we apply the slope correction. The distribution function can be now approximated as

$$\begin{aligned} f(x) = f(x_i) &+ \tfrac{\varepsilon_i^+}{6\Delta x^2}[2(x-x_i)(x-x_{i-\frac{3}{2}}) + (x-x_{i-\frac{1}{2}})(x-x_{i+\frac{1}{2}})](f_{i+1}-f_i) \\ &+ \tfrac{\varepsilon_i^-}{6\Delta x^2}[2(x-x_i)(x-x_{i+\frac{3}{2}}) + (x-x_{i-\frac{1}{2}})(x-x_{i+\frac{1}{2}})](f_i - f_{i-1}) \end{aligned} \tag{1.39}$$

where we omit the dependence on the time. We obtain for the flux :

$$\begin{cases} \Phi_i = a\frac{\Delta t}{\Delta x}[f_i + \frac{\varepsilon_i^+}{6}(1-a\frac{\Delta t}{\Delta x})(2-a\frac{\Delta t}{\Delta x})(f_{i+1}-f_i) + \frac{\varepsilon_i^-}{6}(1-a\frac{\Delta t}{\Delta x})(1+a\frac{\Delta t}{\Delta x})(f_i - f_{i-1})] \\ \\ \Phi_i = a\frac{\Delta t}{\Delta x}[f_i - \frac{\varepsilon_i^+}{6}(1-a\frac{\Delta t}{\Delta x})(1+a\frac{\Delta t}{\Delta x})(f_{i+1}-f_i) - \frac{\varepsilon_i^-}{6}(2+a\frac{\Delta t}{\Delta x})(1+a\frac{\Delta t}{\Delta x})(f_i - f_{i-1})] \end{cases} \tag{1.40}$$

for positive and negative a, respectively. Note that from this definition of the flux, the variation in cell i depends only on the value of the adjacent cells.
The locality of the algorithm enable us to parallelize the code with low effort as explained in detail in section (1.3.5).

1.3.3 Charge conservation

In the fully relativistic electromagnetic 1D case the splitted equations are

$$\begin{cases} \frac{\partial f_1}{\partial t} + \frac{p_x}{M\gamma}\cdot\frac{\partial f_1}{\partial x} = 0 \\ \\ \frac{\partial f_2}{\partial t} + q\left(E_x + (\frac{\vec{p}}{M\gamma}\times\vec{B})_x\right)\frac{\partial f_2}{\partial p_x} = 0 \end{cases} \tag{1.41}$$

We would like to reduce the problem to seek a solution of an advection type equation as eq.(1.25). The eq.(1.41) can be written in the form of advection type equations with source

terms on the r.h.s. as

$$\begin{cases} \partial_t f_1 + \partial_x(\frac{p_x}{M\gamma}\cdot f_1) = f_1 \cdot \partial_x\left(\frac{p_x}{M\gamma}\right) \\ \\ \partial_t f_2 + q\partial_{p_x}\left(\left(E_x + (\frac{\vec{p}}{M\gamma}\times\vec{B})_x\right)\cdot f_2\right) = f_2\cdot\partial_{p_x}(\frac{\vec{p}}{M\gamma}\times\vec{B})_x \end{cases} \tag{1.42}$$

where we use $\gamma = \sqrt{1+\frac{p_x^2+p_y^2+p_z^2}{M^2}}$. The dipendence of eq.(1.42) on γ-factor leads to the appearance of extra terms in the advection equations resulting from the splitting. We can prove that the terms on the r.h.s. of eq.(1.42) vanish in the electrostatic non-relativistic case where $\gamma \simeq 1$ and constant, but they are different from zero in the systems we are interested in.

If we simply apply the methods above presented for the evolution of the distribution function, we totally neglect these terms and a cumulative systematic error would be introduced at each time step. The result would be a poor conservation of the charge density for each species.

In order to be sure that the total particle mass is conserved during each time-cycle the quantities on the right side of the eq.(1.42) can be considered as local source terms in the Vlasov equation. Therefore we should integrate them at each time step and reintroduce all the quantity of mass that these represent, in the corresponding distribution function.

In literature several unsplit methods can be found to ride this difficulty out [7, 8]. Despite that, they would involve a big effort in the numerical implementation, and moreover in all the physical systems in this thesis we refer to, the error turns out to be negligible or otherwise is limited by the following "ad hoc" correction.

Once integration is done in each time step, since we are able to know the position in real axis where we lose charge density, we should re-add this quantity in the phase space reproducing in the momentum space the same distribution of the remaining particles.

Moreover, using equations (1.14, 1.16), we can make explicit the dependence of the γ-factor on the transverse vector potential $\vec{A}_\perp$. In detail, the source terms become

$$\begin{cases} f_1\cdot\frac{p_x}{M}\cdot\frac{\partial}{\partial x}\left(\frac{1}{\gamma}\right) = -f_1\cdot\frac{p_x}{2M^3\gamma^3}\cdot\partial_x|\vec{p}_\perp|^2 \propto -\partial_x|\vec{A}_\perp|^2 \\ \\ f_2\cdot\frac{(\vec{p}\times\vec{B})_x}{M}\cdot\frac{\partial}{\partial p_x}\left(\frac{1}{\gamma}\right) = -f_2\cdot\frac{(\vec{p}\times\vec{B})_x}{M^3\gamma^3}\cdot p_x \propto -\partial_x|\vec{A}_\perp|^2 \end{cases} \tag{1.43}$$

where for the second equation we have used $\vec{B}_\perp = \vec{\nabla}\times\vec{A}_\perp$.

We can infer that, without applying the correction, this error subsists in the region where the electromagnetic effects are important (i.e. in correspondence of the laser pulse where $\vec{A}_\perp \neq 0$). On the other hand, in the region where the transverse potential vector vanishes the system is automatically reduced to the electrostatic case.

In addiction, we can assume that the loss in ion mass is negligible because of the dependence of eq.(1.43) on the mass of the species, and because for the ions the γ-factor is almost a constant $\gamma \simeq 1$ during all the time interval of the simulation. Thus the dynamics of the ions should not be affected by this error. Instead, concerning electron the resulting effect would be a decreasing of the total density, so that the plasma would be no more exactly neutral and a longitudinal electric field would arise.
With the above explained correction this problem is overcome, the dynamics of the particle is not fundamentally modified and the neutrality is preserved.

The described correction is applied to all the simulations showed in this thesis.
As an example, in Fig.(1.3) we report the comparison between a simulation carried out without the correction and a corrected one, running with the same parameters. The simulation will be described in detail in Par.(3.3). The Fig.(1.3) represents the ion density peak and the corresponding longitudinal electric field of a shock wave propagating in an overdense plasma.

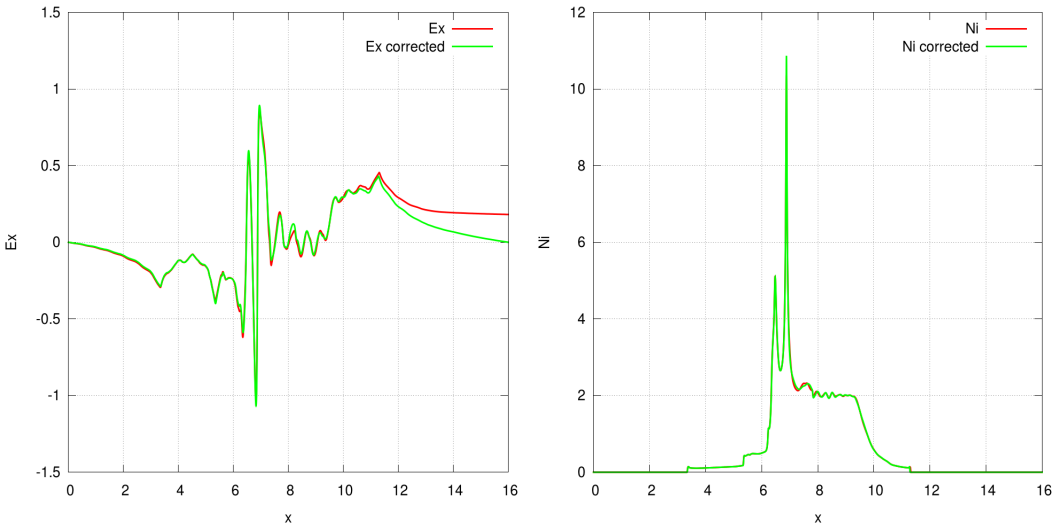

Figure 1.3: Longitudinal electric field (left frame) and ion density (right frame) after 45 periods of interaction of an intense laser pulse with an overdense plasma. Simulation carried out without the correction (red line) and with the correction (green line).

As we can see, if the correction is not applied a longitudinal electric field arises, due to the lost in the electron density that cause the plasma to be non exactly neutral. Reintroducing the lost electron mass, the E_x field vanishes at the end of the box, but the shape of the density is not fundamentally modified, as shown in the figure on the right.

1.3.4 Integration of fields

In the 1D geometry, using the normalized quantities defined in Par.(1.3.6), the Maxwell's equations in Gaussian units become:

$$\begin{cases} \partial_x B_x = 0 \\ \partial_t B_x = 0 \\ \partial_t B_y = \partial_x E_z \\ \partial_t B_z = -\partial_x E_y \end{cases} \qquad \begin{cases} \partial_x E_x = \rho \\ \partial_t E_y = -J_y - \partial_x B_z \\ \partial_t E_z = -J_z - \partial_x B_y \end{cases} \tag{1.44}$$

where $\rho(x,t)$ and $\vec{J}_\perp(x,t)$ are defined in eq.(1.3) and in this 1D case the transverse current density becomes

$$\vec{J}_\perp(x,t) = \sum_\alpha q_\alpha \int \frac{\vec{p}_\perp(x,t)}{m_\alpha \gamma_\alpha} \cdot f_\alpha(x, p_{x,\alpha}, t) \mathrm{d}p_{x,\alpha} \tag{1.45}$$

where the value of the transverse momentum is calculated exploiting the conservation of canonical momentum defined in eq.(1.14).
The required value of the vector potential is provided by $\vec{B}(x,t) = \vec{\nabla} \times \vec{A}(x,t)$ and, since we can consider the laser turned on at $t = 0$, we obtain $\vec{\Pi}_\perp(x, t=0) = \vec{\Pi}_\perp(x,t) = 0$ for each time step.
The longitudinal electric field E_x can be derived by the Poisson equation calculating the integral of charge density in a cell. What we get is the value of E_x at the cell boundaries

$$E_x(x_i + \frac{\Delta x}{2}, t) \quad = \quad E_x(x_i - \frac{\Delta x}{2}, t) + \rho(x_i, t) \cdot \Delta x \tag{1.46}$$

The longitudinal magnetic field B_x is uniform and constant, therefore it is set to zero, that is the required condition for the conservation of transverse canonical momentum.
In order to find a solution for the transverse fields, we need to introduce auxiliary fields that fulfill equations which can be integrated along the characteristic curves $x = \pm t$, recalling that we use $c = 1$. Therefore we must set the value of Δx equal to the time step Δt.

$$\begin{cases} F_\pm = E_y \pm B_z \\ G_\pm = E_z \pm B_y \end{cases} \quad \Longrightarrow \quad \begin{cases} (\partial_t \pm \partial_x) F_\pm = -J_y \\ (\partial_t \pm \partial_x) G_\mp = -J_z \end{cases} \tag{1.47}$$

We obtain an advance scheme expressed by the following relations :

$$\begin{aligned} F_\pm(x \pm \Delta x, t + \Delta t) &= F_\pm(x,t) - \Delta t \cdot J_y(x \pm \tfrac{\Delta x}{2}, t + \tfrac{\Delta t}{2}) \\ G_\pm(x \mp \Delta x, t + \Delta t) &= G_\pm(x,t) - \Delta t \cdot J_z(x \mp \tfrac{\Delta x}{2}, t + \tfrac{\Delta t}{2}) \end{aligned} \tag{1.48}$$

Then we can return to the solution of the physical electromagnetic fields simply by

$$\begin{aligned} E_y = F_+ + F_- \quad ; \quad B_y = G_+ - G_- \\ E_z = G_+ + G_- \quad ; \quad B_z = F_+ - F_- \end{aligned} \tag{1.49}$$

As it is clear from eq.(1.48) the fields are known at the cell boundaries, if we define the discretized current at the cell center and at timesteps $t^{n+\frac{1}{2}} = (n+\frac{1}{2}) \cdot \Delta t$. This is a leap-frog scheme correct up to order $\mathcal{O}(\Delta t^2)$.

1.3.5 Boundary Conditions and Parallelization

We chose different type of boundary conditions for the distribution function and for the fields. In real space, open boundaries are used for fields, whereas two type of boundary conditions are implemented for distribution function, both periodic and reflecting. The algorithm used for the reconstruction of the distribution function allows us to chose the most suitable condition according to the problem we are studying. Other methods, for example those based on the fast Fourier transform of the distribution function in phase space, in case of reflecting condition would generate and then propagate spurious Gibbs oscillations [9].
Boundary conditions in momentum space are even more crucial in order to confine the physical process in a consistent way. So if we allow particles to reach the boundary corresponding to the maximum momentum value, any other acceleration would accumulate more density giving a non physical amount of charge at a fixed position in real space. This might damage the physical result of the field solver.
In Ref.[10] Büchner mentions several possible choices of momentum boundary conditions, such as the introduction of an artificial numerical friction added close to the boundary, but since we are interested in particle acceleration we prefer to set the extent of the grid big enough to contain all the particles. This requires more computational effort. For this reason, we have chosen to parallelize the code.
The method implemented for the evolution and interpolation of the distribution function and the use of a fixed Eulerian mesh, turn out to be really helpful for parallelization purposes with the use of OpenMP (Open Multi-Processing). This is an interface that supports shared memory multiprocessing programming. It makes possible to execute a section of code at the same time on a fixed number of threads associated to different processors. Each thread works on a limited range in the real and momentum axis, and the reconstruction scheme avoids the possibility that more than one thread has to update the value of the same cell. Despite that each thread can read the memory associated to all the other threads.

For example, once we have the distribution function over all the grid, it is possible to calculate the flux at the cell boundaries using OpenMP. Regarding the $(i\,,\,j)$-cell, the calculaion of the new value of the flux in the cell, as defined in eq(1.40), requires to know the distribution function in the adjacent cells, and these values are available also if one of that cells belongs to another thread. However we are sure that no other thread can write in the $(i\,,\,j)$-cell or needs to use the new flux value during the same time cycle.
Moreover, once the range on the grid associated to each thread is fixed, the working load of the threads is constant. This is an important difference with the parallelization of PIC codes, in which the particles can move through the threads and the computational effort of each thread can change during the simulation.

1.3.6 Normalization and scaling of equations

In the code we developed all the physical quantities are normalized as follows.
The mass and momentum of each species are in units of electron mass m_e and $m_e c$, respectively. The normalized charge is defined as $\tilde{q} = \frac{q}{|e|}$.
For the x-axis we chose as normalization length the laser wavelength and for the time the laser period as

$$\tilde{t} = \frac{t}{T} \quad ; \quad \tilde{x} = \frac{x}{\lambda}$$

Thus, the velocity is automatically in units of $\tilde{v} = v\frac{T}{\lambda} = \frac{v}{c}$.
Using Gaussian units for Maxwell's equations, so that the electric and magnetic fields have the same dimensions, we set the normalization for fields and densities as

$$\begin{aligned} \tilde{E} &= \tfrac{eE}{m_e c\omega} \qquad \tilde{\rho} = \tfrac{8\pi^2 e}{m_e \omega^2}\rho \\ \tilde{B} &= \tfrac{eB}{m_e c\omega} \qquad \tilde{J} = \tfrac{8\pi^2 e}{m_e c\omega^2}J \end{aligned} \tag{1.50}$$

where $\omega = \frac{2\pi}{T}$ is the laser pulse frequency.
The equation of the motion of a particle under the action of the Lorentz force, setting $c = 1$, takes the form

$$\frac{dp}{dt} = 2\pi q(E + \frac{p}{m\gamma} \times B) \tag{1.51}$$

where we omit the tilde above all the quantities. The quantity $E_0 = \frac{m_e c\omega}{e}$, that is the units for the fields, can be used to define the threshold above which relativistic effects in the electron dynamics become important. This limit is given in terms of the dimensionless

parameter $a_0 = \frac{E}{E_0} = 1$ with

$$E_0 = 3.2 \times 10^{12} \frac{\mathrm{V}}{\mathrm{m}} \left(\frac{\lambda}{1\ \mu\mathrm{m}} \right)^{-1} \tag{1.52}$$

$$a_0 = 0.85(\frac{I}{10^{18}\mathrm{W} \cdot \mathrm{cm}^{-2}} \cdot \lambda^2_{\mu\mathrm{m}})^{1/2} \tag{1.53}$$

where we express the intensity as $I = \frac{c}{8\pi} \mid E \mid^2$.
The charge density is normalized as $\tilde{\rho} = 2\pi \frac{\rho}{\rho_{crit}}$, where $\rho_{crit} = e n_{crit}$ and n_{crit} is the critical density

$$n_{crit} = \frac{m_e \omega^2}{4\pi e^2} = 1.1 \times 10^{21} \mathrm{cm}^{-3} \left(\frac{\lambda}{1\ \mu\mathrm{m}} \right)^{-2} \tag{1.54}$$

It represents the value over which no propagation in the plasma can occur. A plasma with density $n > n_{crit}$ is said to be "overdense", in the opposite case "underdense".
In the equations we have to solve in the code there are two characteristic parameters: the dimensionless amplitude a_0 and the ratio $\frac{n}{n_{crit}}$. Once fixed these quantities, it is possible to convert the results of a simulation to the physical dimensions in order to relate the simulation with experimental results. Thus we need to set only the value of λ, since both these input parameters depend on the laser wavelength, as defined in (1.53- 1.54).

Chapter 2

Wavebreaking of a wake wave

Significant progress has been made in the last years in the study of laser-plasma based accelerators, Ref.[12]. In these structures electric fields of the order of $\sim 100\ ^{\mathrm{GV}}/_{\mathrm{m}}$ that are orders of magnitude greater than those achievable using conventional methods can be reached. Moreover, they should provide high-performance in a much smaller size than other accelerators.
The first mechanism for utilizing high-intensity laser to accelerate electrons was suggested by Tajima and Dawson in 1979 [13]. The generation of high-energy electrons is associated with laser wake waves, that are density perturbations excited behind a propagating laser pulse in a plasma. In the scheme suggested in [13], the wake is composed of plasma oscillations and the electrons can reach high energy by "surfing" on the waves. Thus, efficient energy transfer between the wave and the particles requires that the particles velocity equal the phase velocity of the wave. We will show that in the case of cold plasmas this corresponds to the wave-breaking limit.
Nowadays, large amplitude plasma waves can be generated, close to the wave breaking threshold, with strong longitudinal electric fields and relativistic phase velocities, which is an efficient way to generate high energy electrons that are injected into the accelerating region and get trapped in the wake waves.

The laser wakefield method is first presented for cold plasmas and then thermal effects are also included, in order to investigate the role of the velocity distribution in the dynamics of the accelerated particles. We will see that in the strongly nonlinear case, the electron density of the wake waves shows a peaky profile, a Dirac's delta function in cold plasma and a peakon-type shape function for thermal plasma. This latter function represents a class of exact solutions of non linear partial differential equations with a discontinuous first derivative [14]. Moreover the investigation on the propagation of peakon-type solutions leads

to the study of a possible application as relativistic "flying mirror" [20], made by the density sheet composed by the accelerated electrons, for a counter propagating laser pulse, as we will discuss in par.(2.2.1).

2.1 Laser wakefields

It can be proved that in a plasma in interaction with the electromagnetic fields of a laser pulse, the evolution with time of the position and velocity of the charged particles, averaged over the period of the laser pulse, can be described by the so called ponderomotive force, defined as

$$\vec{f_p} = -\frac{q^2}{4m\omega^2}\vec{\nabla} \mid \vec{E} \mid^2 = -\vec{\nabla}\Phi_p \tag{2.1}$$

where Φ_p is called ponderomotive potential, that is the cycle-averaged oscillation energy.
In the relativistic regime the ponderomotive force can be expressed, as in Ref.[15], in terms of the relativistic cycle-averaged kinetic energy

$$\vec{f_p} = -\vec{\nabla}(mc^2(\gamma - 1)) = -mc^2\vec{\nabla}(1 + \langle \vec{a}^2 \rangle)^{\frac{1}{2}} \tag{2.2}$$

where $\vec{a}$ denotes the dimensionless vector potential and $\gamma = \sqrt{1 + \langle \vec{a}^2 \rangle}$.
The expression of this force in both eq.(2.1-2.2) represents the slowly-varying term of the total electromagnetic force, and it is related to the envelope of the electromagnetic field of the laser pulse, that is assumed to vary on a time-scale longer than the fast oscillations which have period $T = \frac{2\pi}{\omega}$. Thus, the complete motion of each particle should be a superposition of the two contributions.
Since eq.(2.1) is proportional to the charge squared, both negative and positive charged particles undergo a force in the same direction. The most important feature of the ponderomotive force is that charged particles are expelled from regions where the electric field is more intense. However, regarding ion dynamics, the ponderomotive force is generally negligible because $\vec{f_p}$ scales with the inverse of the particle mass.
In our 1D geometry, the ponderomotive force is a traveling force $f_p(x,t) = f_p(x - v_g t)$ where v_g is the group velocity of the laser pulse, defined as $v_g = \frac{\partial \omega}{\partial k}$.
As showed in Fig.(2.1) a charge separation can be created by the ponderomotive force acting on the electron population, and under suitable conditions, the electrons that are scattered off produce a plasma electron density oscillation. For a laser pulse as the one sketched in Fig.(2.1), the ponderomotive force has two spikes with opposite sign on the rising and falling fronts of the laser pulse, that can enforce the positive, and respectively negative, part of a plasma oscillation. It is known that in a cold plasma the dispersion relation of a plasma waves is simply $\omega = \omega_p$, defining the plasma frequency as $\omega_p^2 = \frac{4\pi n_e e^2}{m_e}$. So, in order to gen-

erate a plasma wave, the optimal condition is obtained for a pulse duration τ_L close to half the plasma oscillation period $T_p = \frac{2\pi}{\omega_p} \simeq 2\tau_L$, such that the second spikes of the ponderomotive force acts on the electrons that have reversed their velocity, enforcing their oscillation, because of the negative sign of the force in the falling ramp of the laser pulse.
Moreover, causality imposes that the plasma oscillations are excited behind the traveling front. Because of that they are named as wake-waves.

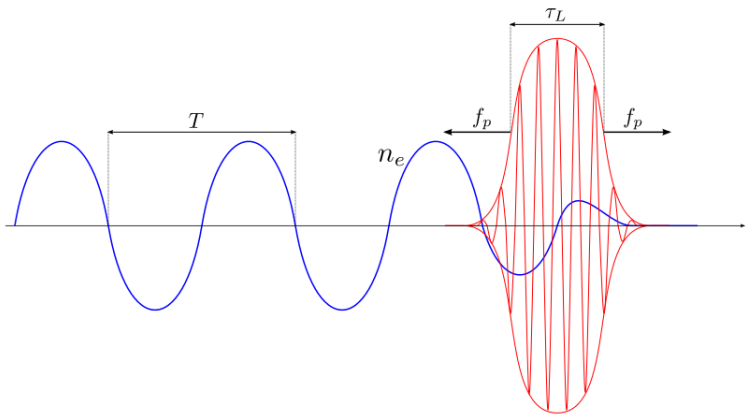

Figure 2.1: Generation of a plasma wake wave. The electron density oscillations (blue line) grow as a wake of the laser pulse (red line) propagating in the positive direction, by the effect of the ponderomotive force f_p.

The plasma wave seems to be the best candidate for an electron acceleration scheme, because of two main properties: it has a non vanishing longitudinal electric field and the phase velocity is determined by how the wave is excited.
This turns out to be a useful feature because in the rest frame of the wake wave all the electrons with velocity close to the phase velocity would face a constant electric field E_x that can provide for a net acceleration, instead of an oscillating field whose acceleration would average to zero over a period.
As the oscillation is produced by the action of the ponderomotive force, the phase velocity of the wave results to be equal to the group velocity of the laser pulse, that is determined in the linear case by the value of the density as $v_g = c\sqrt{1 - \frac{\omega_p^2}{\omega^2}} = c\sqrt{1 - \frac{n_e}{n_{crit}}}$ and considering the relativistic effects that make the refractive index nonlinear, we obtain $v_g = c \cdot \sqrt{1 - \frac{n_e}{n_{crit}\gamma}}$ with $\gamma = \sqrt{1 + \langle a^2 \rangle}$, where a is the dimensionless vector potential and the angular brackets denote the average over an oscillation period.
Electrons trapped in the wake can be accelerated to high energy until they remain in a region with negative electric field. The acceleration process causes a dephasing between the particles

and the plasma wave, since the velocity acquired by the electrons becomes greater than the phase velocity, and the electrons may not suffer anymore an accelerating field. This makes the acceleration method inefficient, but in the relativistic case this problem is overcome since a large change in energy corresponds to a reasonably small change in velocity, and so the dephasing effect is limited.
For this reason we look for a plasma wave with phase velocity as close as possible to c, that can be found since $v_f = v_g \lesssim c$.
If we consider an intense laser pulse that generates large amplitude perturbations, our study cannot be restricted to the linear approximation. Regarding the following relativistic fluid equations

$$\begin{cases} \partial_t n_e + \vec{\nabla}(n_e \cdot \frac{\vec{p_e}}{m_e \gamma_e}) = 0 \\ \\ n_e \left(\frac{\partial \vec{p_e}}{\partial t} + (\frac{\vec{p_e}}{m_e \gamma_e} \cdot \vec{\nabla}) \vec{p_e} \right) = -e n_e \left(\vec{E} + \frac{\vec{p_e}}{m_e \gamma_e} \times \vec{B} \right) \end{cases} \tag{2.3}$$

the nonlinear terms make the wake waves steepen, the profiles of fluid velocity and longitudinal electric field take a sawtooth shape and the profile of the electron density become spiky, as showed in Fig.(2.2).

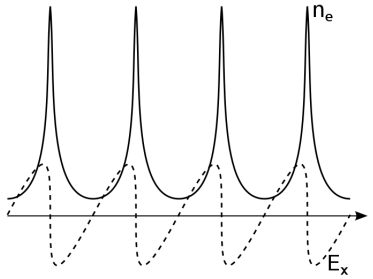

Figure 2.2: Wake waves in the non linear regime. Electron density spikes (solid line) and longitudinal electric field (dashed line) with a sawtooth shape.

In the extreme nonlinear case, the density acquires a Dirac's delta function shape, and the minimum value can be proved to be $n_e = \frac{n_0}{2}$. The longitudinal electric field vanishes in correspondence of a density spike and in the midpoints between two spikes. The region between these two points is the accelerating region where the electrons are trapped.

2.1.1 Wave Breaking

The density perturbation that grows as a plasma wake wave must fulfill some physical restrictions. The total electron density is a positive quantity $n_e = n_0 + \delta n_e \geq 0$, denoting with δn_e the density perturbation of the initial value n_0, thus we obtain $\mid \delta n_e \mid \leq n_0$.

From the Poisson's equation we get a limit on the value of the longitudinal electric field and from the linearized equation of motion a limit on the fluid velocity, as

$$\partial_x E_x = -4\pi\delta n_e \quad \rightarrow \quad \mid E_x \mid = \frac{4\pi \mid \delta n_e \mid}{k_x} \leq \frac{4\pi n_0}{k_x} = \frac{\omega_p v_{ph} m_e}{e} = E_x^{WB} \tag{2.4}$$

$$m_e \partial_t v_x = -eE_x \quad \rightarrow \quad \mid v_x \mid = \frac{e \mid E_x \mid}{m_e \omega_p} \leq v_{ph} \tag{2.5}$$

where we use $v_{ph} = \frac{\omega_p}{k_x}$, and we assume the linear approximation to be valid. Despite of the large use of these relations in literature and the fact that the wave breaking threshold turns out to be correct in the non-relativistic regime, we must notice that here it is assumed that the wave remains sinusoidal, which is not correct because the wave in nonlinearly steepened as it approaches the wavebreaking limit. In addition for our case since the wake wave has a velocity $v_f = v_g \lesssim c$ and also the oscillation velocity is close to c, the wave breaking process requires the use of a relativistic approach.

The maximum value for the electric field calculated with a relativistic approach following Ref.[16] is found to be $E^{WB} = \frac{m_e \omega_p c}{e}\sqrt{2(\gamma_{ph} - 1)}$.

Multiplying both sides of eq.(2.5) for the period of the plasma wave the inequality can be expressed as $\lambda_p = \frac{2\pi}{k_x} \geq \frac{2\pi}{\omega_p} v_x$. This means that the oscillation amplitude of the electrons can not exceed one plasma wavelength. When a longitudinal wave goes beyond such limits, the periodic structure may be lost and the wave is said to break. This happens when the fluid velocity equals the phase velocity of the plasma wave and the accelerated particles overtake the wave itself.

The equality between the two velocities represents the optimal phase condition for the acceleration. For this reason in the last decades several studies has been focused on the development of an efficient way to give the electrons the optimal phase for the acceleration. The first approach evaluates the possibility of a stimulated injection of electrons with the desired phase, by exploiting the ponderomotive action of a counterpropagating pump laser pulse [17]. The other approach is based on self-injection, since in a plasma wave close to the wave breaking threshold there is always a fraction of particles constituting the wave that moves at the phase velocity. These electrons are accelerated by the wave itself and self-trapping occurs. This makes clear the importance of driving the wave close to the wave breaking limit for the electrons acceleration, since if the wave is well above this threshold a large part of electrons overpass the wave itself. In this case the regular wave structure is lost and the acceleration method is no more efficient. So, reaching the wave breaking limit we can increase both the energy and fraction of electrons self-trapped in the wave.

2.2 Thermal plasma

Adapting the definition of wavebreaking for the study of warm plasmas is by no means straightforward. In general terms in a thermal distribution there is always a fraction of particles attaining a velocity larger than the phase velocity of the wave. Except for the case in which the plasma finishes in front of the wave, these particles will for sure get trapped, but as long as the wave structure remains unaffected, the wave cannot considered to be broken. This is showed by Bergmann and Mulser in Ref.[18], where they present the results of Vlasov simulations in which fast electrons are generated by trapping but the wave is still regular and periodic, while in the case that a large fraction of electrons gets trapped the periodic structure is lost.
The thermal distribution often used in order to compute analytic calculation is the so so-called waterbag distribution. This model imposes a sharp cut, in the form of an upper and a lower boundary, on the particle momentum distribution, such that the presence of particles with initial momentum beyond the wave breaking limit is avoided.
Within this model we can define the wavebreak of a wave moving at relativistic velocity in the positive direction as occurring with the trapping of the particles of the upper waterbag boundary, so that the greatest value of the particle momentum distribution becomes larger at the wavebreak position than the phase momentum of the wave defined as $p_{ph} = m_e \gamma_{ph} v_{ph}$.
In Ref.[19] the authors take into account a thermal plasma in a 1D geometry with initial distribution function for the electron population showed in Fig.(2.3). This distribution function can be analytically written as $f_e(x, p_x, t) = f_0 \cdot \theta(p_x - p_-(x,t)) \cdot \theta(p_x - p_+(x,t))$, where f_0 is a constant and θ is the Heaviside function.

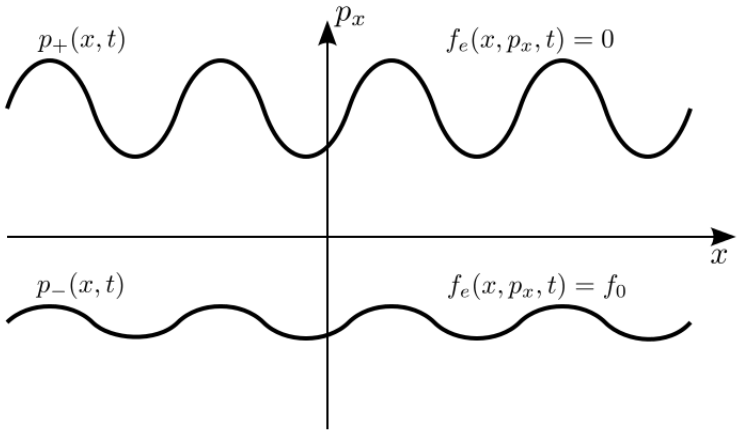

Figure 2.3: Initial waterbag distribution function.

The electron density calculated as first momentum of the distribution function becomes

$$n_e(x,t) = \int_{-\infty}^{+\infty} f_e(x,p_x,t)\mathrm{d}p = f_0(p_+(x,t) - p_-(x,t)) \tag{2.6}$$

The Vlasov-Poisson equations system is solved in a fixed homogeneous ion density background. The equations resulting from the substitution of the chosen distribution function in the Vlasov-Poisson equations are

$$\begin{cases} \partial_t p_+ + \frac{p_+}{\sqrt{1+p_+^2}}\partial_x p_+ = -E \\ \partial_t p_- + \frac{p_-}{\sqrt{1+p_-^2}}\partial_x p_- = -E \\ \partial_x E = 1 - f_0(p_+ - p_-) \end{cases} \tag{2.7}$$

Regarding a plasma wave with constant phase velocity, we can express each quantity in terms of the variable $X = x - v_{ph}t$. Defining the variables $h_\pm(p_\pm)$ as

$$h_\pm(p_\pm) = \sqrt{1+p_\pm^2} - \beta_{ph}p_\pm \tag{2.8}$$

the system of equations (2.7) becomes

$$\begin{cases} h'_+ = -E \\ h'_- = -E \\ E' = 1 - \frac{p_+(h_+) - p_-(h_-)}{\Delta p_0} \end{cases} \tag{2.9}$$

where the prime refers to the derivation respect to X and $\Delta p_0 = p_+(X_0) - p_-(X_0)$ calculated at a fixed $X = X_0$ where $E' = 0$.
The momentum $p_\pm$ as a function of $h_\pm$ can be obtained inverting eq.(2.8). Since h_+ and h_- are not independent because of the first two equations of (2.9), it is possible to reduce the system using the relation $h_- = h_+ + \Delta h_0$, where Δh_0 is a constant determined by the value of $p_\pm(X_0)$ and related with the temperature of the plasma. Now the two remaining equations constitute a Hamiltonian system with canonical variable h_+ and $-E$, with the Hamiltonian function defined as

$$\begin{cases} h'_+ = -\frac{\partial H}{\partial E} \\ E' = -\frac{\partial H}{\partial h_+} \end{cases} \quad \rightarrow \quad H(E,h_+) = \frac{E^2}{2} + \Pi(h_+) \tag{2.10}$$

where the potential $\Pi(h_+)$ is given by

$$\Pi(h_+) = h_+ \left(1 - \frac{\gamma_{ph}^2 \beta_{ph} \Delta h_0}{\Delta p_0}\right) + \frac{W(\gamma_{ph} h_+) - W(\gamma_{ph}(h_+ - \Delta h_0))}{2\Delta p_0} \tag{2.11}$$

$$W(z) = z\sqrt{z^2 - 1} - \ln(z + \sqrt{z^2 - 1}) \tag{2.12}$$

In the system (2.10) we have that the potential $\Pi(h_+)$ is not well defined if $h_+ \to \gamma_{ph}^{-1}$, then we obtain that the upper bound curve of the momentum distribution is no longer a single valued function of X if

$$p_+ \to p_+^{WB} = \frac{\beta_{ph}}{\sqrt{1 - \beta_{ph}^2}} \tag{2.13}$$

This correspond to the wavebreaking limit when the wave forms a region with multi-stream electron motion.

In Ref.[19] the expression for the density is reported and the value at the wavebreak n_e^{WB} is calculated for an initial symmetric distribution function. In order to study the behavior of the density in the neighborhood of the wave breaking, that means $\delta X = X - X^{WB} \to 0$, an expansion on the upper bound momentum curve is performed. Keeping only the first order terms we have

$$p_+ \approx p_+^{WB} - \delta p_+ \qquad n_e \approx n_e^{WB} - \tfrac{\delta p_+}{\Delta p_0} \tag{2.14}$$

where Δp_0 is the momentum width of the distribution function at $t = 0$, and the difference between the maximum momentum and the wave breaking momentum is proved to be

$$\delta p_+ = \sqrt{n_e^{WB} \gamma_{ph}^3} \mid \delta X \mid \quad \to \begin{cases} p_+ \approx p_+^{WB} - \sqrt{n_e^{WB} \gamma_{ph}^3} \mid \delta X \mid \\ \\ n_e \approx n_e^{WB} - \frac{\sqrt{n_e^{WB} \gamma_{ph}^3}}{\Delta p_0} \mid \delta X \mid \end{cases} \tag{2.15}$$

This type of wave breaking, also called "Λ-type" breaking, corresponds to the "peakon" shape solution because the corresponding density peak is a continuous function with a discontinuity in the first derivative.

Eq.(2.15) should be compared with the behavior of the electron momentum and density in the case of wave breaking in a cold plasma with initial conditions $p_{\pm,0} \to 0$. Thus, considering the wave structure in the vicinity of the breaking position, we find

$$\begin{cases} p = p^{WB} - \beta_{ph}^{\frac{1}{3}} \gamma_{ph}^2 (\frac{3}{\sqrt{2}} \mid \delta X \mid)^{\frac{2}{3}} \\ \\ n_e \approx n_0 \gamma_{ph} (\frac{\sqrt{2}}{3} \beta_{ph} \mid \delta X \mid)^{-\frac{2}{3}} \end{cases} \tag{2.16}$$

The electron density tends to infinity as already mentioned.
In the context of laser wakefield acceleration, the interest is focused on the maximum value of the electric field that can be achieved before wavebreak. Bulanov et al. in Ref.[19], prove that approaching the wave breaking, this value is smaller in the case of thermal plasma than the relativistic limit for the cold plasma mentioned in the previous paragraph.
Thus, Bulanov et al. reveal that thermal effects tend to reduce the maximum wave amplitude and modify the structure of the singularity found in the cold plasma limit. This is of great interest for the application as "Flying mirror", since the efficiency of the reflection is strongly dependent on the shape of the density peak.
In section (2.3) we will investigate the onset and development of a wavebreak process of a plasma wave in a warm plasma, and we will show the novel features of the phase space structure after the wavebreaking related with the relativistic particle kinematics.

2.2.1 Flying Mirror

The investigation on the generation of ultrashort pulses in the X-ray spectral region is of interest for many important applications, such as attosecond spectroscopy and imaging. A frequency upshift method is required to make the pulse duration lying in the attosecond regime and to obtain high intensities, focusing the high frequency pulse in an extremely small surface.
A first method has been presented in Ref.[20], where Bulanov et al. suggest the use of thin plasma sheets generated as wakefield for reflection of an external pulse.
In the strongly nonlinear wake wave close to the wavebreaking limit the spiky modulations of the electron density, propagating nearly at the speed of light, can act as relativistic flying mirrors. A counterpropagating laser pulse can be partially reflected by these density foils so that both the frequency and the intensity are increased. We regard the simple case of a reflecting plane surface moving at velocity $V = \beta \cdot c$ where an incident wave with frequency ω in the laboratory frame impinges with $\vec{k}$ parallel to the surface normal vector. The double Doppler effect makes the frequency of the reflected wave to increase by the following factor

$$\omega_r = \omega \frac{1+\beta}{1-\beta} \simeq 4\gamma^2 \omega \tag{2.17}$$

where we consider $\beta \to 1$ since in our case the electron sheets move at $v_{ph} \simeq c$, so that $\gamma = \gamma_{ph} \gg 1$.
Regarding a cold plasma, the importance of using wake wave close to the wavebreaking threshold is illustrated in Ref.[21] where the authors point out the key role of the electron density discontinuity in calculating the reflection coefficient for the one dimensional case.

If the wake wave is far from this limit, its reflectivity is exponentially small. As the wave-breaking is reached, the geometric optics approximation is no longer valid, since the electron density tends to infinity as reported in eq.(2.16). The reflection coefficient, defined as the ratio between the reflected and the incident energy flux, increases and can be expressed, respectively in the mirror rest frame and in the laboratory frame, as reported in Ref.[20] within the assumption of a Dirac delta density shape

$$R' \simeq \frac{1}{2\gamma_{ph}^3}\left(\frac{\omega_d}{\omega}\right)^2 \quad \rightarrow \quad R \simeq 8\gamma_{ph}\left(\frac{\omega_d}{\omega}\right)^2 \tag{2.18}$$

where ω is the frequency of the counterpropagating pulse and ω_d is the frequency of the driver pulse that generates the wakefield.

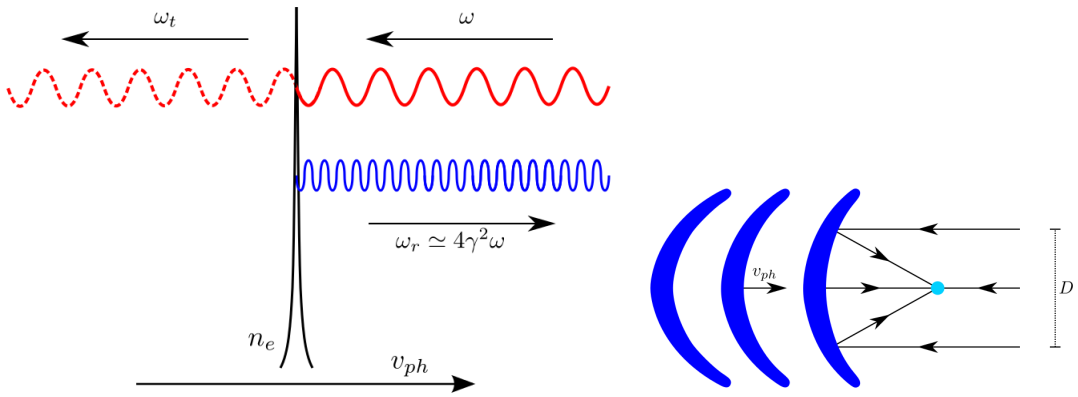

Figure 2.4: Schematic representation of the Flying Mirror concept. Left frame: incident wave (solid red line) on a electron density sheet n_e moving with relativistic speed, transmitted (dashed red line) and reflected (blue line) waves. Right frame: 2D configuration, the parabolic fronts of the electron density (blue) reflect and focus a counterpropagating laser pulse.

The idea of this possible use of flying mirrors was developed in a more realistic three-dimensional configuration, in which the non linear wake wave has a parabolic front, as schematically represented in Fig.(2.4) and proved in Ref.[22]. Indeed, because of the dependence of the γ relativistic factor on the pulse transverse non uniform profile, in the strongly non linear wake waves both the amplitude and the wavelength depend on the distance from the axis.

This leads to an additional effect of intensity increasing, since a parabolic mirror focus the incoming radiation up to a factor $\sim \frac{D}{\lambda'}$, where D denotes the effective diameter of the laser pulse that the parabola can focus, and λ' is the wavelength in the rest frame of the mirror.

This factor can be written in our case as

$$\frac{D}{\lambda'} \simeq 2\gamma_{ph}\frac{D}{\lambda} \tag{2.19}$$

Considering the frequency increasing and the focusing effect, in Ref.[20] Bulanov et al. illustrate as this method allows to achieve extremely high electromagnetic field up to the Schwinger limit, the critical field for quantum electrodynamics at which the vacuum breaks down and pair creation occurs, with the present-day laser technology.
Reaching such an intense field might be difficult experimentally because of several non linear effects, acting during the interaction of the laser pulse with the mirror, that are not taken into account in the paper. Despite that in Ref.[23] some promising results are reported, in agreement with the theoretical expectations. Kando et al. observe laser light reflected with the frequency upshifted by a factor $37 \div 66$, corresponding to the extreme ultraviolet wavelength, with a mirror reflectivity of $R' = (0.3 \div 2) \times 10^{-5}$ in the mirror rest frame.
Recent studies of Bulanov et al. [24] focus on wakefield generation in thermal plasmas, where the electron density in the wake wave does not tend to infinity as in the cold case, but within the assumption of a water-bag distribution, it is described by the solution reported in eq.(2.15). Also in a thermal plasma the shape of the electron density peak provides a finite reflection coefficient. However, this value is extremely sensitive to the density peak shape, that in turn strongly depends on the thermal effects.
The analytical calculation of the reflection coefficient is reported in Ref.[24], in the presence of a thermal broadening of the distribution function represented by the water-bag distribution. Moreover, within this approach Bulanov et al. prove that the reflection coefficient can be substantially increased by reaching the above wavebreaking regime, with respect to the value found for a wake wave approaching that threshold.

2.3 Results

In this paragraph we present numerical studies carried out to prepare the ground for further investigations, aimed to verify the theoretical predictions reported in literature with the assumption of the water bag model. For this reason, our attention is focused on the interaction of an intense laser pulse with an underdense thermal plasma, that is a plasma with background density $n < n_{crit}$ defined in eq.(1.54), with a broad initial distribution function. We run a simulation to test that, since the response of the ions is on a time scale much longer than the electron one, it does not affect the dynamics of the electrons. For this reason, we present the behavior of the electrons lying in a fixed neutralizing ion background.
In order to resemble a water bag distribution we use a distribution function with a rather

flat plateau followed by a fast drop, defined as

$$f(x, p_x, t = 0) = C \cdot g(x) \cdot e^{-(\frac{\alpha p_x^2}{2})^4} \tag{2.20}$$

with $\alpha = \frac{m_e c^2}{T_e}$, where the temperature is chosen such that the electrons do not have a relativistic initial momentum. The function $g(x)$ defines the spatial shape, we opt for a linear rising and falling ramp, and a plateau of variable length. We adopt a smooth front density rise $8\,\lambda$ long, so as to reduce the disturbance caused by the pulse entering the plasma from the vacuum region.
The normalization constant C fixes the density to the value of $n_e = \frac{1}{16} n_{crit}$ so that the group velocity of the propagating pulse is $v_g \simeq 0.98\,c$ for a laser amplitude $a_0 = 1.8$. The laser pulse has a temporal profile with $\sin^2$-like rising and falling ramp of two periods length. We use a high resolution for the space grid and for the time step, as $\Delta x = \Delta t = \frac{1}{1000}\lambda$, and the extension of a cell in the momentum space is $\Delta p_x = 0.03\, m_e c$.
The density value is chosen in order to obtain the optimal condition for the generation of plasma wave as wake of a laser pulse with $\tau_L = 2T$, thus we expect the period of the wakewave to be $T_p \simeq 4T$. The wavebreaking momentum can be calculated as $P^{WB} = m_e v_{ph} \gamma_{ph}$, that gives a value of $\sim 5\, m_e c$.

2.3.1 Peakon type solution

In this paragraph we present simulations carried out to study the shape of the density peaks growing as a wake. In order to verify how the thermal effects act in the wavebreaking regime, we make a comparison with a PIC code simulation initialized with cold plasma, with a resolution of $\Delta x = \frac{1}{100}\lambda$ and $N_p = 1000$ particles per cell.
In Fig.(2.5) we show the electron phase space resulting from a Vlasov code simulation with $\alpha = 100$, that means $T_e \simeq 5\,\mathrm{KeV}$. In the left frame the plasma wave has not yet reached the breaking momentum, on the contrary in the right frame the electron momentum go beyond the breaking value P^{WB}.
We can observe that in the PIC simulation, where each macroparticle is represented by the red dot in the phase space in Fig.(2.5), with the initial condition of cold plasma the wave does not break since the particles do not reach the breaking momentum $P^{WB} \simeq 5\, m_e c$. This points out that the wavebreaking process and the generation of relativistic electrons, are an effect of the thermal spread of the initial distribution.
Contrary to the water-bag case we expect that the absence of a sharp momentum cut in the initial distribution makes the density and its space derivatives continuous, although very steep.

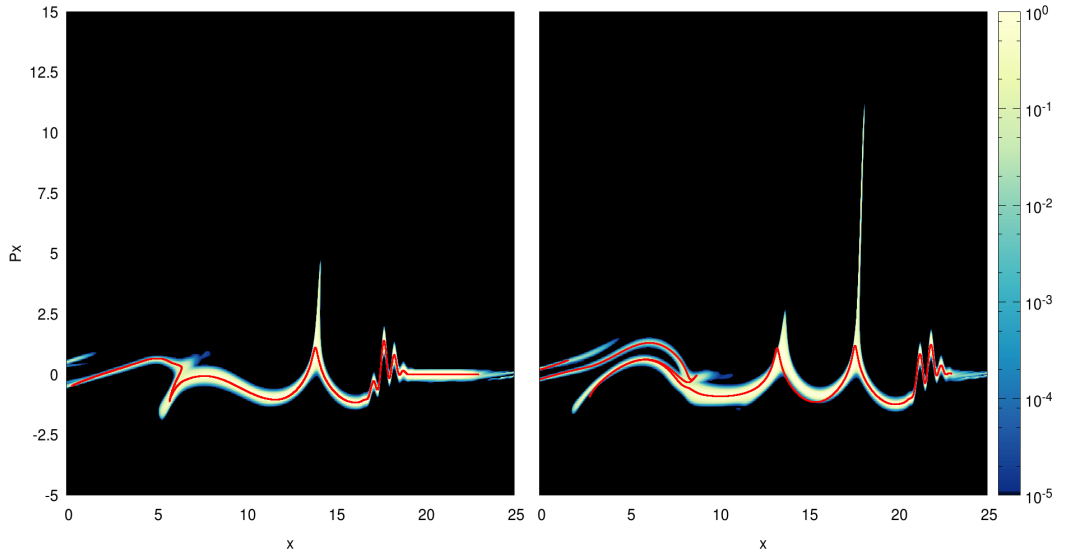

Figure 2.5: Electron phase space distribution function after 16, 20 periods of interaction with the laser pulse. Red dots, distribution function of a cold plasma performed with the PIC code.

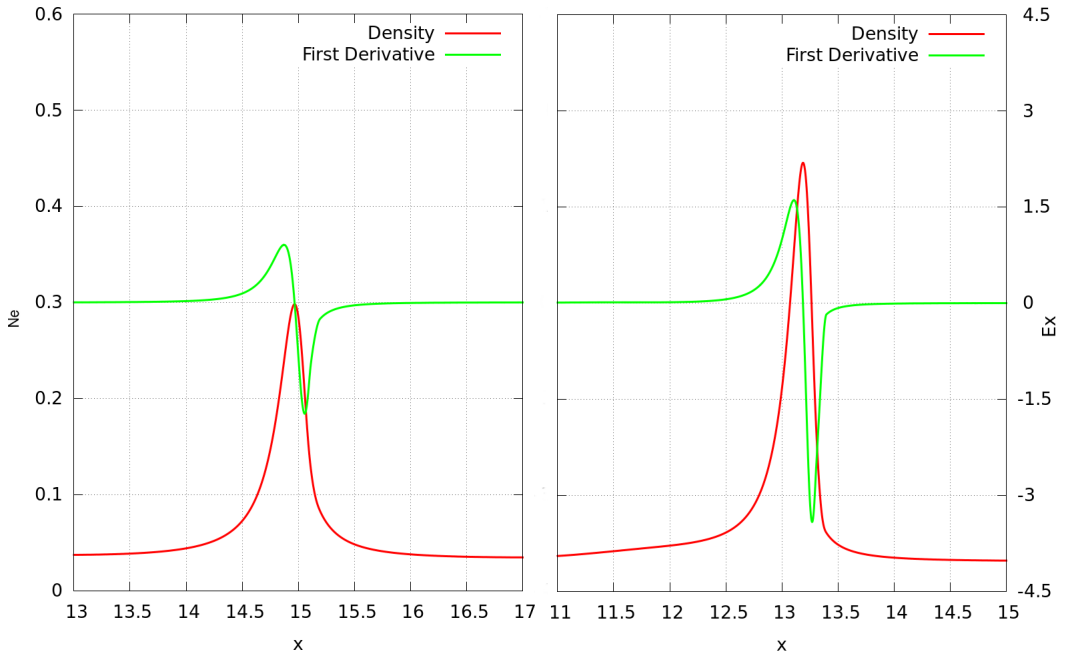

Figure 2.6: Electron density peak (red line) and its first derivative (green line) close to the wavebreaking. Left frame: laser amplitude $a_0 = 1.8$, time step showed corresponding to 17 T. Right frame: laser amplitude $a_0 = 2.5$, time step showed corresponding to 12 T.

The electron density reaches a maximum value of ~ 5 times the initial density after 17 periods, as showed in the left frame of Fig.(2.6). For comparison we report also the density peak of a simulation carried out with maximum field amplitude $a_0 = 2.5$. It exhibits a more spiky peak, with a greater maximum density value, up to ~ 7 times the initial density.
Both the peak shapes resemble the expected peakon-type solution. We show also the first derivative of the density and we can see that this quantity approaches the discontinuity as theoretically predicted.

2.3.2 Folding of the phase space

Now we focus on the above wavebreaking regime, since we want to investigate the behavior and the persistence of the density spike.
In Ref.[19] thanks to the assumption of a waterbag distribution Bulanov et al. prove that above the wavebreaking threshold, in case of warm plasma, the density singularity can face an electric field greater than the relativistic limit found by Akhiezer and Polovin in Ref.[16]. Moreover, since the velocity of the density peak in the frame of the wake wave is $\simeq \frac{c}{2\gamma_{ph}^2}$, with $\gamma_{ph} \gg 1$, the density peak can exist for a long time of the order $t_{acc} \simeq \lambda_w \frac{2\gamma_{ph}^2}{c}$ where λ_w denotes the wake wave wavelength.
Bulanov et al. in Ref.[19] study the dynamics of electrons that have bypassed the wake wave, without considering the selfconsistent modification of the electric field which may affect the propagation.
The aim of this paragraph is to analyze the above wavebreaking regime, specifically the effect of ultra-relativistic kinematics on the injection process and trapping of the electrons into the wake wave. Since numerically we can account for the selfconsistent modification effect, here we report the results of a simulation that runs with a mesh of length $65\,\lambda$, within an interval in the momentum space as $-10 < \frac{p_x}{m_e c} < 50$.
All the other parametersare kept as defined for the simulations presented in Par.(2.3.1).
In Fig.(2.7) a portion of the simulation box is shown in order to point out the wavebreak structure in the left frame at $x \simeq 25\lambda$. It is possible to describe this first stage of wavebreaking with a model of single particle dynamics. We can consider the electrons with $p_x > p_{ph}$ move ballistically following $x(t) = \beta t$, so that in the phase space we obtain

$$p_x(x) = \frac{x}{\sqrt{\bar{t}^2 - x^2}} \quad \text{for} \quad \frac{p_{ph}\bar{t}}{\sqrt{1+p_{ph}^2}} < x < \frac{p_{max}\bar{t}}{\sqrt{1+p_{max}^2}} \tag{2.21}$$

at a fixed time $t = \bar{t}$, where p_{max} denotes the maximum momentum reached by the accelerated particles. This dependence corresponds to an accumulation of electrons in the region of the phase space around $x \to \bar{t}$.

In the simulation we observe that the value of p_{max} increases with time, due to the presence of a negative electric field. Therefore we add in this model a constant acceleration related to $E_0 < 0$. This leads to an increase of the electrons momentum while their velocity is only slightly changed. With this assumption, we obtain the implicit relationship

$$-E_0 x(\bar{t}) = \sqrt{1 + p_x^2} - \sqrt{1 + (p_x + E_0 \bar{t})^2} \tag{2.22}$$

which gives a phase plot with a spiky structure similar to the one described by relation (2.21) with a greater momentum p_{max}. Eq.(2.22) mimics the initial time interval after the wavebreak as showed in the left frame of Fig.(2.7) but does not reproduce the shape of the distribution function of all the accelerated electrons for the successive time steps.
As we can see in the central and right frame, as the wavebreak process evolves this model remains valid only for the electrons with the largest values of the momentum that carry on propagating in the local minimum of the electric field.

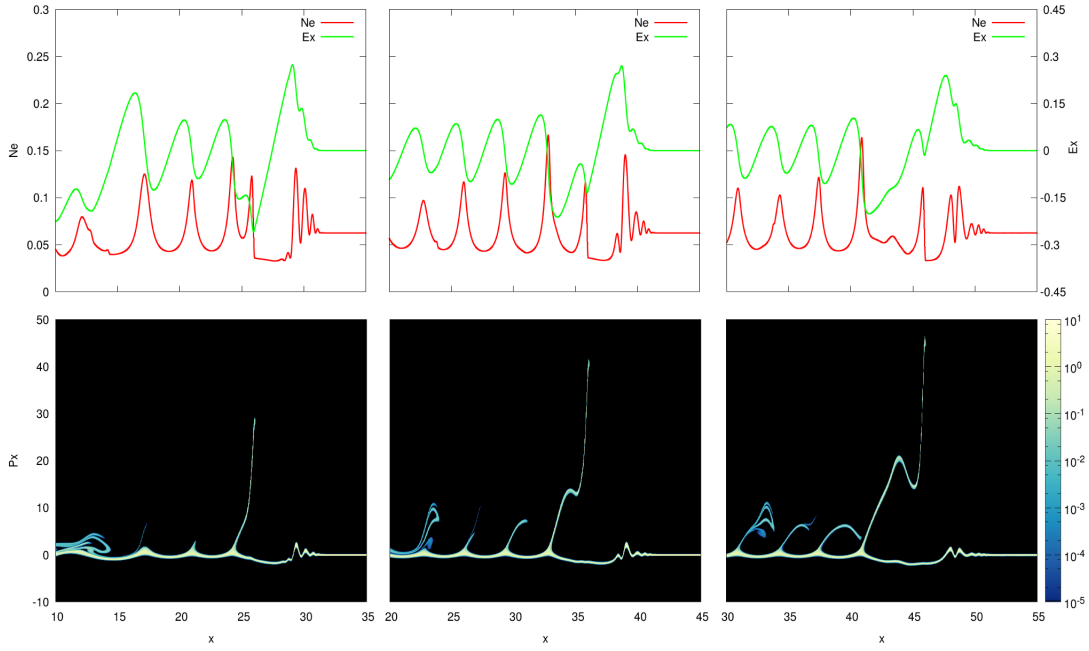

Figure 2.7: Top: Electron density (red line) and longitudinal electric field (green line). Bottom: Electron phase space distribution function at $t = 28\,T$ (left frame), $t = 38\,T$ (central frame) and $t = 48\,T$ (left frame).

This simple model does not account for the self consistent modification caused by the electrons injected in the relativistic wake wave, that change the wave structure by producing a relative maximum in the electric field in the accelerating region where the value of E_x is

negative. As we can see in the central frame in Fig.(2.7) around $x \simeq 35\,\lambda$ the electrons behind this local maximum experience a more negative field than the electrons in front of it and are thus accelerated faster. This greater acceleration for the electrons behind the maximum increases their momentum producing a folding in momentum space but it does not significantly affect their trajectory, as we can note the shape of the density spike and its steep rise is not drastically modified.

Later in time the local maximum of the electric field vanishes and then turns positive, so that the electrons in that region are decelerated and start to be trapped in the potential of the wave, as showed in the right frame. The electrons with the largest momentum keep propagating in a region with negative electric field for a longer time, but even these at a time not showed here enter in a region with positive electric field and start decelerating.

This behavior is different from what observed under non relativistic conditions where the injected electrons with larger momenta have proportionally larger velocities and thus simply reach the decelerating electric field region proportionally faster than the particles with smaller momenta.

An important consequence of the relativistic kinematic is the long lasting electron density steep rise at the wavebreak position, corresponding to the electrons with highest momentum. Indeed, despite of their significantly different momenta, they propagate almost with the same velocity in the laboratory frame. The maximum value of the density jump occurs at the earlier time, being $0.44\frac{n_{crit}}{\lambda}$ at $t = 26\,T$, and then the peak widens due to the phase space folding, reducing to $0.34\frac{n_{crit}}{\lambda}$ at $t = 62\,T$.

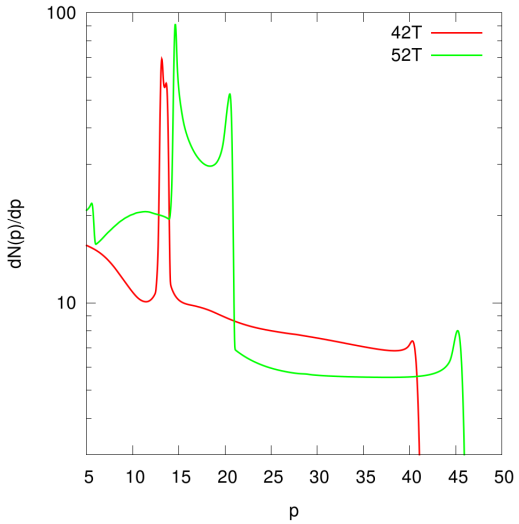

Figure 2.8: Momentum spectrum of the electrons with $p_x > p_{ph}$ at $t = 42, 52\,T$.

In Fig.(2.8) the momentum spectrum is shown for electrons with momentum greater than the wave breaking value, lying in the x-range around the first broken wake wave. The double horned structure corresponds to the electrons in the folds in momentum space of the central and right frame of Fig.(2.7). The fraction of electrons of the first wake wave that go beyond the wavebreaking threshold is $\sim 14\%$ at $t = 42\,T$ and $\sim 21\%$ at $t = 52\,T$, relative to the unperturbed density in a region of the same length of the one considered around the wake wave.

Qualitatively similar results have been observed in a simulation which runs with $\beta_{ph} = 0.9$, obtained using an external driver in order to represents the ponderomotive effect of the laser pulse. The wave breaking momentum in this case is $p^{WB} \simeq 2\, m_e c$, and accordingly the maximum momentum reached by the electrons in smaller than in the above discussed case. The folding of the phase space distribution is similar but takes place at intermediate values of p_x, the trapping of the injected electrons with the highest momentum starts on a shorter time scale.

2.3.3 Comparison with PIC code simulations

We run a simulation using the PIC code with parameters as close as possible to the Vlasov simulation presented above. In the PIC simulation we use a number of particles per cell $N_p = 1000$ and a resolution on the space grid $\Delta x = \frac{1}{100}\lambda$.

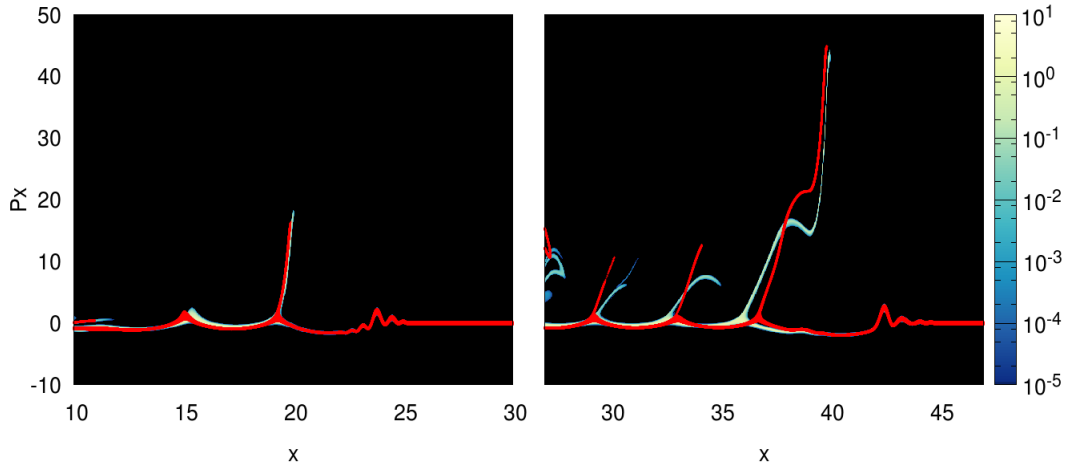

Figure 2.9: Electron distribution function for the Vlasov and PIC (red dots) simulation at $t = 26,\ 46\,T$.

In Fig.(2.9) we show two phase space snapshots where the results obtained with our Vlasov code are compared with those obtained with the PIC code. We superimpose the macropar-

ticles (red dots) of the distribution function resulting from the PIC simulation to the phase space of the Vlasov simulation at two time steps.
This comparison provides a test of the correctness of the developed Vlasov code in the relativistic and electromagnetic regime. As a consequence of the use of a Time Splitting Method, a poor mass conservation may affect our numerical solution in the region of the phase space where the vector potential is non vanishes, as showed by the eq.(1.43). However, in the region corresponding to the laser pulse, i.e. where $\vec{A}_\perp \neq 0$, there is a substantial overlap of the two phase spaces. For this reason we assume that the applied correction, described in Par.(1.3.3), works properly. Moreover, we can deduce that the differences behind the laser pulse are not associated with this problem of the Vlasov code algorithm.
In the left frame of Fig.(2.9) we observe that at the early stage of wavebreaking there is a good agreement also in the wake wave structures. Then the differences arise in the wake waves, where the PIC code produces a sharper structures than the Vlasov simulation. These differences let us infer that the distribution function play a key role in the dynamics of the accelerated particles. Despite of that, we observe the folding of the first wake wave with both the numerical methods and, also at later time not showed here, all the phase space structures are qualitatively well reproduced.

Chapter 3

Collisionless shock acceleration

A shock wave is a propagating solution of the hydrodynamics equations that involves a change in the macroscopic plasma state. It appears as a transition layer across which the fluid variables, such as density and velocity, are discontinuous.
In the last years, collisionless shock waves in laser-produced plasmas attracted increasing interest as a concept for the laser-driven acceleration of ions, since a shock wave performs an acceleration of a part of the ions population by reflecting it at the shock front surface. Several studies are now focused on the potential applications in, e.g. radiobiology and medicine (such as hadron therapy and isotope production). Most of these applications would require a ion beam with a sufficiently narrow energy spread; on this side, recent experimental studies on laser shock acceleration have given promising results, which we discuss below.
The study of acceleration of charged particles by collisionless shock waves is also important in the astrophysical context, for example in order to understand cosmic ray acceleration.
The laser intensities reached nowadays open the way for innovative experiments that can emulate the conditions of the astrophysical phenomena in the laboratory. In Ref.[25] a theoretical and numerical study of the nature of collisionless shock waves is presented in order to clarify the different conditions that lead to an electrostatic or electromagnetic shock waves. The first type has been widely studied in laboratory experiments of laser-plasma interaction, the other one is usually relevant in the astrophysical scenario. Stockem et al. in Ref.[25] discuss on the possibility to reproduce in the laboratory with the state-of-the-art laser systems the condition to generate electromagnetic shock waves and thus to understand the underlying physics connected with the astrophysics observations.
Beyond the simple theoretical model that we will present, this acceleration method has been investigated with simulations [26, 27, 28] and experiments [29]. In Ref.[29] the observation of proton beams up to $\sim 22\,\mathrm{MeV}$, with an energy spread of $\frac{\Delta E}{E_{\mathrm{FWHM}}} < 1\%$, is attributed to the generation of a collisionless shock driven by the laser-heated electrons.

The experimental setup is showed in Fig.(3.1): a CO_2 laser pulse with wavelength $\lambda = 10\,\mu$m interacts with hydrogen gas targets. With this wavelength value, it is possible to produce an overdense plasma also from the ionization of a gas target. The accelerated ions are then detected by a stack of five CR39 detectors, placed at a distance of 15 cm from the plasma. This detector is a plastic polymer in which a colliding ion leave a trail of broken chemical bonds, this track can be etched putting the detector in a concentrated alkali solution.
The number of ions is then counted and the energy calculated by measuring the distance traveled through the plastic. Comparing this value with the Bragg peak penetration length of a proton, the ion energy is obtained.

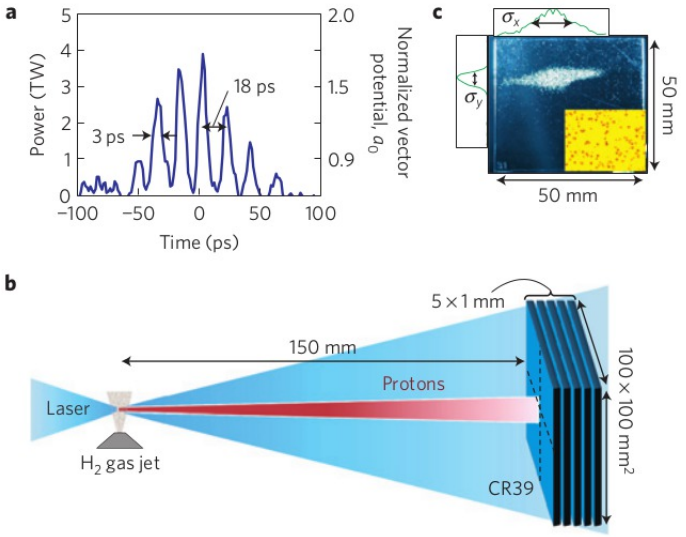

Figure 3.1: Ref.[29]. (a) Temporal profile of the CO_2 laser pulse as measured by a streak camera. (b) Representation of the experimental setup. (c) Proton beam detection on the fourth CR39 detector.

The number of detected protons reported in Ref.[29] is $\sim 10^7\,\mathrm{MeV}^{-1}\mathrm{sr}^{-1}$, this value is orders of magnitude below from what is observed with a similar set-up, still using gas jet targets and CO_2 laser pulses, by Palmer et al. in Ref. [30]. The observed spectra of both the experiments are reported in Fig.(3.2). With the use of a magnetic spectrometer Palmer et al. detect a number of protons of $\sim 3\times10^{12}\,\mathrm{MeV}^{-1}\mathrm{sr}^{-1}$, with a maximum energy of $\sim 1\,$MeV and energy spread of $\frac{\Delta E}{E_{\mathrm{FWHM}}} \simeq 4\%$.
The great difference between the data from the two experiments is due to the physical mechanism behind the acceleration process. In this latter experiment the laser pulse is circularly polarized, so that the electron heating is reduced, as we will explain in Par.(3.2.1), and the shock can not be launched by the laser-heated electrons as in Ref.[29], where the

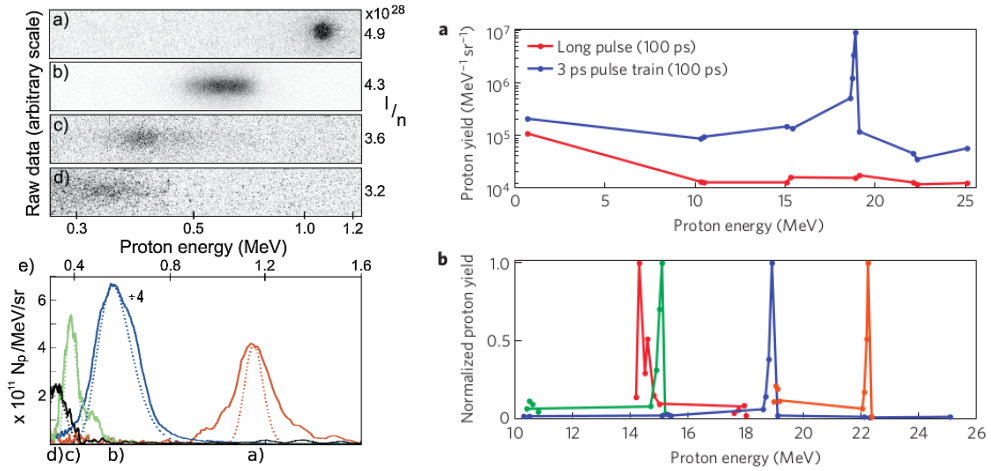

Figure 3.2: Left frame Ref.[30]: Proton energy spectra for different value of I/n. Top: Raw data. Bottom: Background subtracted (solid line) and corrected spectra (dashed line). Right frame Ref.[29]: (a) Proton energy spectra obtained with the modulated pulse (blue line) and with a smooth pulse (red line), both containing 60 J. (b) Energy spectra obtained with different amplitude of the laser pulse $a_0 = 1.5 \div 2.5$.

authors use a linearly polarized laser pulse. Therefore, the acceleration is associated with the piston effect of the radiation pressure, that acts as snowplow reflecting a large fraction of ions. This mechanism is also named as "Hole Boring" acceleration [31].

The energy value reported in Ref.[29], observed with a so narrow spread, is a remarkable result that has paved the way to many research activities devoted to a detailed comprehension of the physics phenomena they have observed. Our studies have also been motivated by this experiment, in particular the small number of reflected ions let us infer that the Vlasov code might be a necessary tool for the investigation, since we have already mentioned the limit of the PIC code in these cases.
In the next sections, we review the basic theory of collisionless shock in a plasma. As it will turn out, the formation of an electrostatic shock may require the onset of the ion reflection, while in the case of no reflection solitary wave solutions are found.

3.1 Ion acoustic solitary waves

In this paragraph we present the Sagdeev pseudo-potential method [32] in order to describe a ion-acoustic soliton and prepare the ground for seeking a shock solution. This method fully account for nonlinearities because it is not perturbative, and for this reason can be applied

to large amplitude waves.
When the wave amplitude becomes large enough that the linear approximation breaks down, nonlinear effects must be taken into account. In a finite amplitude wave the nonlinearities cause the wave to steepen, and this steepening in a collisionless plasma can be limited by dispersion effects. The case in which these effects balance each other, leads to the generation of a solitary wave structure, or simply a soliton, that can propagate over a large distance keeping the original shape.
We are interested in solitons related to the ion acoustic waves, so we consider a population of cold ions ($T_i = 0$) and warm electrons of temperature T_e. The ion dynamics is described by the fluid equations

$$\partial_t n_i + \partial_x(n_i v_i) = 0 \quad ; \quad \partial_t v_i + v_i \partial_x v_i = \frac{q_i}{M_i} E \tag{3.1}$$

where n_i is the ion density, v_i is the fluid velocity, and we limited our studies to the 1D case. From this point forward, we consider for simplicity the ions charge $q_i = Ze = e$, i.e. an electron-proton plasma.
Eq.(3.1) should be solved together with Poisson's equation

$$\partial_x E = 4\pi e(n_i - n_e) \tag{3.2}$$

Assuming the electrons to be in equilibrium with the electric potential $\phi(x,t)$, defined as $E_x = -\partial_x \phi$, and with the thermal pressure P_e, and choosing an isothermal closure for the fluid equations, as

$$\begin{cases} m_e n_e \partial_t v_e = e n_e \partial_x \phi - \partial_x P_e = 0 \\ P_e = n_e K_B T_e \end{cases} \tag{3.3}$$

we obtain for the density a Boltzmann equilibrium as $n_e = n_0 e^{\frac{e\phi}{K_B T_e}}$, where n_0 denotes the unperturbed density value.
We look for solutions with constant profile in the frame in which the wave is at rest. Thus, if we study the problem in the reference system of the wave solution, moving with velocity V_s relative to the laboratory frame, we have $\partial_t = 0$ and we obtain

$$\begin{cases} \partial_x(n_i v_i) = 0 & \rightarrow \quad n_i v_i = -n_0 V_s \\ v_i \partial_x v_i = -\frac{e}{M_i}\partial_x \phi & \rightarrow \quad \frac{1}{2} M_i v_i^2 + e\phi = \frac{1}{2} M_i V_s^2 \end{cases} \tag{3.4}$$

In this frame we see a stream of plasma impinging on the wave front. Since we set $T_i = 0$, the ions are at rest in the laboratory system, so all the particles constituting the flux have the same velocity $-V_s$.

The first of eq.(3.4) represents the conservation of the density flux, the second one the conservation of the energy for ions crossing the solitary wave potential.
We can derive the velocity from the first of (3.4) and substitute it in the second one, in order to find a relation between the density and the scalar potential as

$$n_i(x) = n_0 \left(1 - \frac{2e\phi(x)}{M_i V_s^2}\right)^{-\frac{1}{2}} \tag{3.5}$$

Since we want to keep the density value non negative, we find out a condition for the electric potential $e\phi(x) \leq \frac{1}{2} M_i V_s^2$. This means that the ions have enough kinetic energy to overtake the potential barrier of the soliton. If this condition would not be meet and a reflection would start, since all the ions are cold and so have the same velocity in the wave frame, all of them would get reflected. In the range of the acceptable values for the potential, there exists a critical value defined as $e\phi_{crit} = \frac{1}{2} M_i V_s^2$.
We can close our system of equations using Poisson's equation with the above defined density

$$\frac{\partial^2 \phi}{\partial x^2} = -4\pi e \left(\frac{n_0}{\sqrt{1 - \frac{2e\phi(x)}{M_i V_s^2}}} - n_0 e^{\frac{e\phi}{K_B T_e}} \right) = -\partial_\phi \Psi(\phi) \tag{3.6}$$

This equation can be regarded as a single particle equation moving in a potential well. Within this analogy, we should consider ϕ as the position, x as the time variable and $\Psi(\phi)$ would be the so called Sagdeev pseudo-potential. We are interested in studying the value acquired by the pseudo-particle position during its oscillatory motion inside the well.
We can start integrating once eq.(3.6), we obtain

$$\frac{1}{2} \left(\frac{\partial \phi}{\partial x} \right)^2 + \Psi(\phi) = K \tag{3.7}$$

$$\Psi(\phi) = -4\pi n_0 \left[M_i V_s^2 \sqrt{1 - \frac{2e\phi(x)}{M_i V_s^2}} + K_B T_e e^{\frac{e\phi}{K_B T_e}} \right] \tag{3.8}$$

where K is the integration constant and can be included in the value of $\Psi(\phi)$.
The most interesting case for us is the one with the integration constant set to the particular value $K = 4\pi n_0 (M_i V_s^2 + K_B T_e) = \Psi(\phi(x \to \infty))$, so that we obtain

$$\left. \frac{d\Psi}{d\phi} \right|_{\phi=0} = 0 \quad ; \quad \Psi(\phi = 0) = 0; \tag{3.9}$$

We impose also that $\Psi(\phi \to 0) < 0$ to ensure that Ψ is a well, and $\Psi(\phi_{crit}) > 0$ in order to have a maximum value at the intersection with the ϕ-axis. With the conditions (3.9)

the pseudo-particle needs an infinite time to complete an oscillation in the pseudo-potential well. Thus, the solution of the equation of motion in the well is a unique oscillation that represents the soliton. Moreover, the two conditions lead to a limited range in which the soliton solution exists. Explicitly, the soliton propagation velocity must exceed ion-acoustic velocity $c_s = \sqrt{\frac{K_B T_e}{M_i}}$, but the value of the Mach number defined as $\mathcal{M} = \frac{V_s}{c_s}$ has to be included in the range $1 < \mathcal{M} < 1.6$.
In Fig.(3.3), we show the solution obtained with these choices.
The pseudo-particle starts from $\phi = 0$, it arrives at the maximum value ϕ_m and it goes back by taking the same path. It is a totally symmetrical solution and so the background ions do not change their fluid state. Without the first of conditions (3.9) we would obtain a nonlinear wave-train.

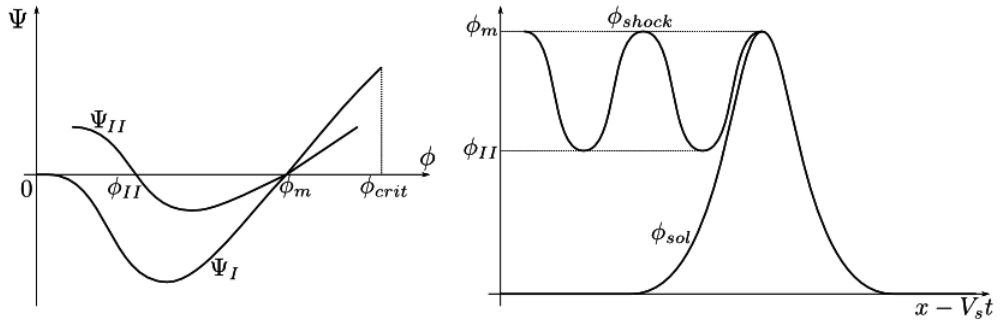

Figure 3.3: Left frame: Sagdeev pseudo-potential well for the soliton $\Psi_{\rm I}(\phi)$, and for the shock solution. Right frame: electric potential of the soliton and shock solution.

3.2 Collisionless Shock Waves

Until now we have neglected all the dissipation and kinetic effects. In this paragraph we show how to find analytically a collisionless shock wave solution, with constant velocity and maximum amplitude, assuming the electrons to be in Boltzmann equilibrium.
In order to produce a shock wave starting from the basic fluid theory as in the previous paragraph, we need a non symmetrical pseudo-potential as sketched in Fig.(3.3). We show that a possible way to destroy this symmetry is allowing for ions reflections at the shock front and that the reflection is an intrinsic feature for the shock wave development and not an outcome effect. Following Ref.[32] we illustrate how the existence of ions reflected by the shock front is sufficient to obtain formally a shock wave solution.
In order to allow for ion reflection, it is necessary to define a non monoenergetic ion distri-

bution function $f_i(x, v, t)$. For example, it could be a Maxwellian distribution with a width determined by the thermal velocity that is fixed once we specify the ion temperature $T_i \neq 0$, keeping $T_i \ll T_e$.
As done before, we treat the problem as stationary in the wave frame, so the condition for the ions to get reflected becomes

$$e\phi(x) \geq \frac{1}{2} M_i v_i^2 \tag{3.10}$$

where v_i denotes the velocity of the ions in the reference system moving with velocity V_s. The reflection occurs for all the ions whose kinetic energy does not exceed the potential energy at the shock front.
The density of ions that can not overtake the potential barrier $\phi(x)$ can be expressed, considering for simplicity $v_i = v - V_s$, as

$$F(\phi) = \frac{1}{n_0} \cdot \int\limits_{\frac{1}{2} M_i (v - V_s)^2 \leq e\phi(x)} f_i(x, v, t) \mathrm{d}v \tag{3.11}$$

So all the particles with velocity in the same direction of the shock propagation are more easily reflected than the other particles.
Defining x_m as the position of the maximum value of the electrostatic potential ϕ_m we can label the "upstream" region $x > x_m$ where the shock has not yet passed through as region I, and the "downstream" region $x < x_m$ as region II. We can make a model of the reflected ions contribution considering the ion density in the unperturbed region I as $n_{i,I}(x \to +\infty) = n_0(1 + F(\phi_m))$, and the same for the electron density in order to ensure the neutrality of the plasma. Moreover, in the first of eq.(3.4) the conservation of flux that crosses the shock front is modified as $n_i v_i = n_0(1 - F(\phi_m))V_s$. We are not allowing for other possible reflections in region II. In eq.(3.6) we can add the terms referred to the reflected ions, obtaining:

$$\begin{aligned}
&\text{I}: && \frac{\partial^2 \phi}{\partial x^2} = -\frac{\partial \Psi_{\mathrm{I}}}{\partial x} = -4\pi e n_0 \left[\frac{1 - F(\phi_m)}{\sqrt{1 - \frac{2e\phi(x)}{M_i V_s^2}}}) + 2F(\phi) - (1 + F(\phi_m)) e^{\frac{e\phi}{K_B T_e}} \right] \\
&\text{II}: && \frac{\partial^2 \phi}{\partial x^2} = -\frac{\partial \Psi_{\mathrm{II}}}{\partial x} = -4\pi e n_0 \left[\frac{1 - F(\phi_m)}{\sqrt{1 - \frac{2e\phi(x)}{M_i V_s^2}}} - (1 - F(\phi_m)) e^{\frac{e\phi}{K_B T_e}} \right]
\end{aligned} \tag{3.12}$$

following the same procedure of eq.(3.7) we get an equation for each region:

$$\frac{1}{2} \left(\frac{\partial \phi}{\partial x} \right)^2 + \Psi_{I,II}(\phi) = K_{I,II} \tag{3.13}$$

We seek a solution for ϕ continuous in $x = x_m$,thus the integration constants must be chosen

so that the pseudo-potentials fulfill $\Psi_I(\phi_m) = \Psi_{II}(\phi_m)$ as in Fig.(3.3).
The analogy with the motion of a single particle in a potential well can be made again. The particle makes a first oscillation in the potential well defined by $\Psi_I(\phi)$, reproducing the same shape of the first half part of a soliton, and then oscillates indefinitely between ϕ_m and $\phi_{\rm II}$, as showed in Fig.(3.3).
Therefore, if an electrostatic shock starts propagating in a Maxwellian plasma, we expect that some reflected ions will always be produced and that the momentum acquired by the reflected ions will be twice the propagation momentum of the shock front. As long as V_s is constant, the spectrum of reflected ions should be quasi mono-energetic.
The ions gain energy from the wave, so we should expect to see a damping in the shock that we do not take into account in this model because of the assumption of stationary profile solution. This is a good approximation in case of $F(\phi_m) \ll 1$, which means that a small fraction of ions are reflected.

3.2.1 Hot electron generation

The collisionless shock waves we investigate on, are driven by laser-heated electrons that penetrate inside the plasma. The generation of high energy electrons in the interaction of an intense laser pulse with an overdense plasma has been the subject of several experiments, since it is the most important mechanism of energy transport inside the target. From now on, we will refer to these high energy electrons as fast or hot electron.
In Ref.[33] Brunel suggests an electrostatic model to explain hot electron generation in case of P-polarized intense laser pulse with oblique incidence on a plasma with step-like density shape. In an overdense plasma the electromagnetic fields are evanescent and penetrate only in a thin layer of length of the order of the skin depth $l_s = \frac{c}{\omega_{p,e}}$. The electrons lying in this layer are heated up, the thermal expansion entails a charge separation, and an electric longitudinal field E_x arises, back-holding the electrons which attempt to escape in the vacuum. However, if the laser pulse is such intense that the electric field E_L is larger than E_x, the electrons of the plasma can be dragged out in vacuum for about half a cycle of the laser pulse by means of the electric field component perpendicular to the surface. In detail the condition for vacuum heating is equivalent to a laser intensity being so intense that the ponderomotive force is strong enough to overcome the thermal expansion, so that the plasma density is steepened near the critical surface, which brings consistence with the assumption of a step-like density profile. The electrons are then pushed back inside the plasma, where they deliver the energy acquired during the oscillation in the vacuum region. For this reason, this mechanism of hot electron generation is usually referred to as Vacuum Heating.
In Ref.[33] an external capacitor field in the longitudinal direction, extending on the vacuum side only, is taken into account to resemble the ponderomotive effect. This simplified model

allows us to understand the pulsed nature of the hot electron bunches, that in this case are generated once per each laser cycle. In Fig.(3.4) we show the trajectories of the electrons moving across the plasma-vacuum interface in a 1D geometry.

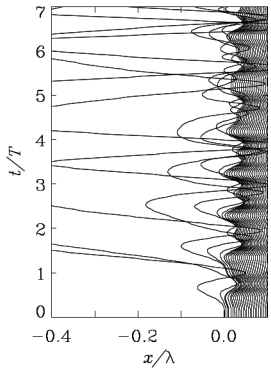

Figure 3.4: The figure shows the trajectories of electrons (more rigorously of fluid elements) in the simple electrostatic model where an oscillating capacitor field, roughly representing the laser pulse action, is applied across the interface of a step-density plasma [34]: it is observed that some electrons re-enter at high velocity into the plasma after oscillating for half a cycle on the vacuum side.

An analogous heating mechanism is found considering the magnetic term of the Lorentz force, since $\vec{v} \times \vec{B}$ has a component perpendicular to the plasma surface. This mechanism leads to the generation of two bunches of hot electrons per laser cycle, as schematically reported in Fig.(3.5). The $\vec{v} \times \vec{B}$ Heating is the dominant mechanism in case of S-polarization and normal incidence, since the electric field of the laser pulse does not have a component perpendicular to the plasma surface.

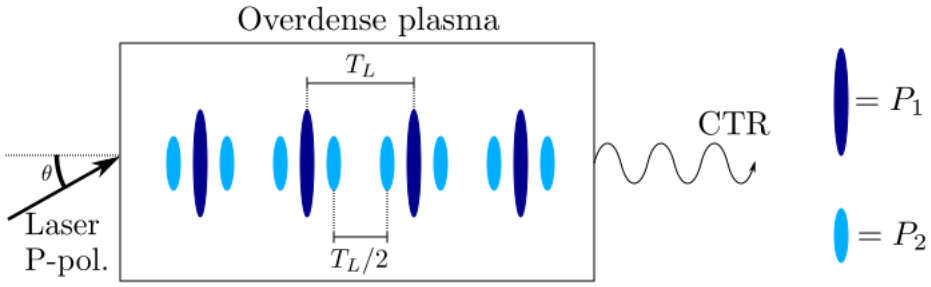

Figure 3.5: Schematic representation of the interaction of an intense laser pulse P-polarized on an overdense plasma. The hot electron generation is due to the Vacuum Heating and to the $\vec{v} \times \vec{B}$ Heating respectively with frequency ω (bunches P1) and 2ω (bunches P2). At the rear side of the plasma CTR refers to the Coherent Transition Radiation.

In order to show that in this case the bunches are generated with a periodicity 2ω, we consider as example a cold plasma with a step-like density shape interacting with a S-polarized laser pulse. For the sake of simplicity, we refer to the non relativistic case within the linear approximation regime. The vector potential inside the plasma can be expressed as

$$\vec{a}(x,t) = \frac{a_0}{\sqrt{1+\varepsilon^2}} e^{-\frac{x}{l_s}} \left(\hat{y} \cdot \cos(\omega t) + \varepsilon \hat{z} \cdot \sin(\omega t)\right) \tag{3.14}$$

where ε represents the polarization, linear for $\varepsilon = 0$ and circular for $\varepsilon = 1$.
The longitudinal force component becomes

$$F_x = -m_e c^2 \partial_x \frac{\mid \vec{a} \mid^2}{2} = F_0 e^{\frac{-2x}{l_s}} \left(1 + \frac{1-\varepsilon^2}{1+\varepsilon^2} \cos(2\omega t)\right) \tag{3.15}$$

Within a perturbative approach, we can linearize the fluid equations that describe the electron dynamics, i.e. equation of motion, Poisson and continuity equations, and keeping only the terms oscillating at 2ω frequency, we obtain

$$\delta n_e^{(2\omega)} = \frac{2}{l_s} \frac{n_0}{m_e} F_0 e^{\frac{-2x}{l_s}} \frac{1-\varepsilon^2}{1+\varepsilon^2} \frac{1}{\omega_p^2 - 4\omega^2} \cos(2\omega t) \tag{3.16}$$

$$e E_x^{(2\omega)} = F_0 e^{\frac{-2x}{l_s}} \frac{1-\varepsilon^2}{1+\varepsilon^2} \frac{\omega_p^2}{\omega_p^2 - 4\omega^2} \cos(2\omega t) \tag{3.17}$$

The equations (3.16-3.17) point out the resonant condition for the electron oscillations in case of $\omega_p = 2\omega$. Thus, we expect the electrons to quickly gain energy from the laser pulse and propagate inside the plasma as bunches with dominant frequency 2ω. In Fig.(3.6) we show in advance the electron distribution function resulting from a simulation that will be discussed in the following Par.(3.3.1). We report the portion of the phase space corresponding to the electrons propagating in the forward direction, and the red line on top represents the density oscillations that show with quite good agreement the $\frac{\lambda}{2}$ periodicity.
From eq.(3.15) it is clear that there is a different generation mechanism as ε varies, explicitly with a circularly polarized laser pulse the oscillating term vanishes and so the fast electron generation is suppressed.
An estimation of the order of magnitude of the fast electron kinetic energy in case of linear polarized laser pulse, can be calculated as

$$E_p = m_e c^2 \left(\sqrt{1 + \frac{a_0^2}{2}} - 1\right) \tag{3.18}$$

Since the reflection of the laser pulse from the overdense plasma surface may generate a standing wave with vector potential $\vec{a}(x,t) \simeq \vec{a}(x)\cos(\omega t)$ in the vacuum region, the gained

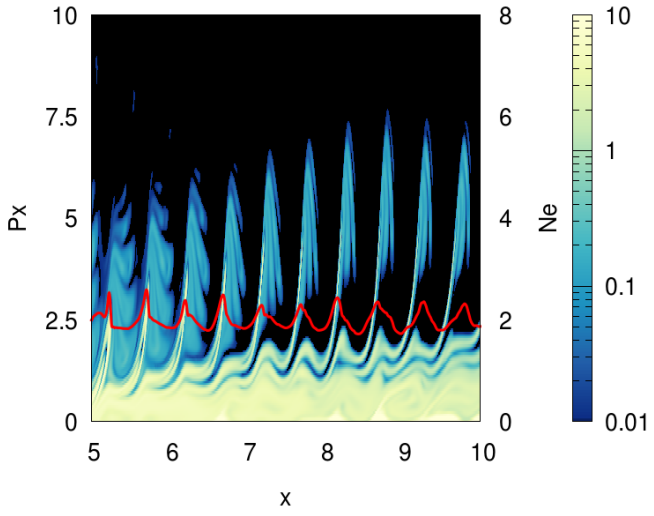

Figure 3.6: Portion of the simulation box of the electron phase space corresponding to the hot electrons propagating in the positive direction. The electron density (red line) shows the oscillation with periodicity $\sim \frac{\lambda}{2}$.

energy can be related to the ponderomotive potential $\Phi_p \simeq -m_e c^2(1 + \langle \vec{a}^2 \rangle)^{\frac{1}{2}}$ defined in Eq.(2.2). As an example, we obtain that the energy gained in the vacuum region and released in the plasma is of the order of $E_p = 0.73\,\mathrm{m_e c^2} \simeq 0.37\,\mathrm{MeV}$, applying a laser pulse with amplitude $a_0 = 2.0$.

The bunches of fast relativistic electrons propagate through the plasma conserving the periodic structure as has been confirmed in Ref.[35] by measurements of the coherent transition radiation (CTR) emitted from the rear surface when the bunches cross it. The observation of CTR reveals the temporal coherence of the electron bunches and that it is conserved during the propagation through the target. Popescu et al. find out the presence of peaks at both the laser frequency and its second harmonic, associated with electrons with energy greater than 2 MeV superimposed on a broad spectrum, for targets with thickness ranging from 20 μm to 1000 μm. The fast electrons propagate inside the plasma and when they reach the rear side, they can not escape because of the electrostatic confinement, so they are pushed back and carry on recirculating across the target.

In the study of soliton or shock solutions, as already seen in Par.(3.1-3.2), the pulsed nature of the hot electrons is usually neglected and a model with a Maxwellian distribution, with a width related to the high energy reached by the fast electrons, is assumed for the energy transport inside the plasma. In the next paragraph we will present an effect that depends strongly on this pulsed nature of hot electrons and so can not be explained by the previous model.

3.2.2 Hole Boring acceleration

A process that may account for ion acceleration at the front surface of an overdense plasma due to the radiation pressure of the impinging laser pulse, is the so-called Hole Boring mechanism.
The ponderomotive force of the laser pulse acts on the electron population at the plasma-vacuum interface pushing them inward in the target and so it generates an electron density peak. Thus a longitudinal electric field which may balance the effect of the ponderomotive force is created due to the space charge displacement.
As in the example presented in the previous paragraph (3.2.1) that starts with the definition of the vector potential in eq.(3.14), we describe the electron dynamics during the interaction by the linearized fluid equations and the Poisson's equation. Expressing the ponderomotive force as the time independent term of eq.(3.15), we find as zero frequency solution

$$eE_x = F_0 e^{\frac{-2x}{l_s}} \tag{3.19}$$

$$\delta n_e = \frac{1}{2\pi e^2}\frac{1}{l_s} F_0 e^{\frac{-2x}{l_s}} \tag{3.20}$$

Thus, the ponderomotive force exactly balances the longitudinal electric field and the electron density varies in a surface layer of the order of the skin depth. The ions are accelerated by means of this electric field component at the front surface causing the steepening of the density profile. The velocity of the surface density can be estimated by a flow momentum balance in relativistic regime as

$$\frac{2I}{c}\frac{1-\frac{v_{\rm HB}}{c}}{1+\frac{v_{\rm HB}}{c}} = n_i \gamma_{\rm HB}(2M_i\gamma_{\rm HB}v_{\rm HB})v_{\rm HB} \tag{3.21}$$

where the left side term is the momentum carried out by the laser pulse and the term on the right is the ion momentum flow, with $\gamma_{\rm HB} = (1-\frac{v_{\rm HB}^2}{c^2})^{-\frac{1}{2}}$. Solving for the Hole Boring velocity we obtain

$$\frac{v_{\rm HB}}{c} = \frac{\Pi^{\frac{1}{2}}}{1+\Pi^{\frac{1}{2}}} \quad \text{with} \quad \Pi = \frac{I}{M_i n_i c^3} = \frac{Z}{A}\frac{n_{crit}}{n_e}\frac{m_e}{M_i}a_0^2 \tag{3.22}$$

The above relations are based on a stationary picture. A dynamical model of the Hole Boring, taking into account charge separation effects, is discussed in Ref.[36]. The model supposes a step-like density profile and a cold plasma, in addition to the use of a circularly polarized laser pulse in order to reduce the effect of thermal expansion and heating of the electron population as described in Par.(3.2.1).
As schematically represented in Fig.(3.7), by taking spatial ad hoc profile for the density

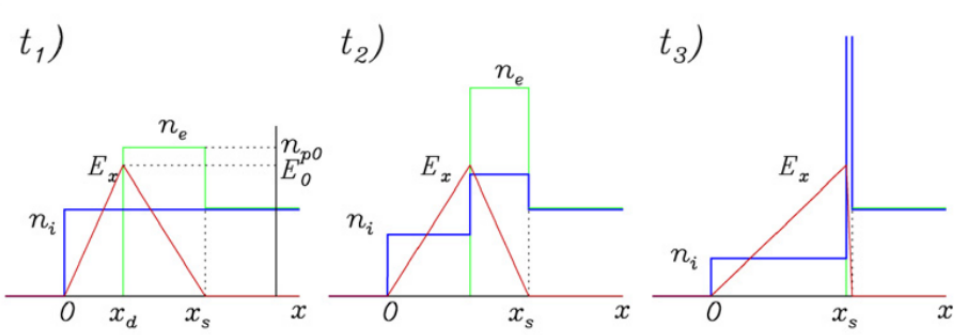

Figure 3.7: Schematic representation of the Hole Boring acceleration mechanism as presented in Ref.[31].

and assuming that the equilibrium condition is maintained by the electrons during the ions motion, the ions in a position $x < x_s$ start moving in the positive direction. Exploiting the conservation of the energy and of the momentum and the charge conservation it is possible to relate the parameters n_{p0}, E_0, x_d and x_s defined in Fig.(3.7). The force acting on the ions lying in the region between x_d and x_s can be expressed as

$$F = eE_0(1 - \frac{x_0 - x_d}{x_s - x_d}) \tag{3.23}$$

with x_0 the ion initial position. Thus solving the equation of motion, all these ions are found to reach the position x_s at the same time. For this reason, an ion density peak rises and the hydrodynamic description breaks down as showed in the right frame of Fig.(3.7). Because of the breaking of the ion density peak, a bunch composed by the fastest ions propagates inside the target with velocity v_{MAX}, which can be obtained from the equation of motion and it results $v_{\mathrm{MAX}} \simeq 2v_{\mathrm{HB}}$. The model provides a good estimation of the velocity value and of its scaling with the laser parameters, although a self-consistent non stationary solution is not available and the description of the dynamics of the breaking is based mostly on numerical simulations.

One of the main difference between this acceleration mechanism and the reflection from the shock front described in Par.(3.2), is that this process accelerates all the ions lying in a layer at the front surface, not only the most energetic ones. Thus we expect an ion high-density bunch, composed by a greater number of particles with respect to the density of particles accelerated by the shock wave. This is consistent with the high density peak observed by Palmer et al. [30] and with the difference between the peak amplitude in the energy spectrum associated with the two described acceleration mechanisms showed in Fig.(3.2).

As explained in Ref.[31] the use of a circularly polarized laser pulse represents the optimal

condition to observe this process. Indeed for linear polarization the strong electron heating and the oscillating component of the longitudinal force may change the efficiency of the piston effect at the surface and the conditions during the wave breaking stage.

3.3 Results

The previous paragraph shows that in the intense laser-plasma interaction either solitons or shocks may be generated. This makes clear the importance of the initial velocity distribution of background ions, that also determines the fraction of reflected particles.
From the relation (3.10) we can calculate that the ions, whose kinetic energy does not exceed the potential barrier of amplitude ϕ_m, have velocity

$$v_i > V_s - \sqrt{\frac{2e\phi_m}{M_i}} \tag{3.24}$$

Once we know the propagation velocity of the shock, since the maximum value of the electrostatic potential is a function of V_s, the condition (3.24) gives the threshold velocity for the ions to get reflected. In order to obtain accelerated particles we should have a distribution function that is extended in the momentum space beyond this threshold value. Thus, in stationary condition, the fraction of reflected particles can be calculated as in eq.(3.11).
In the simulation presented below, we regard a laser pulse impinging on an overdense electron-proton plasma. The distribution function for each species has a Gaussian shape in momentum space, and it is defined as

$$f_\alpha(x, p_x, t = 0) = C_\alpha \cdot g(x) \cdot e^{-(\frac{p_x}{\sqrt{2}\sigma_\alpha})^2} \tag{3.25}$$

where C_α is a normalization constant, and $g(x)$ describes the density profile. We use a steep density profile with a linear rising and falling ramp of length $0.2\,\lambda$. The width of the distribution function in momentum space is related to the temperature by $\sigma_\alpha = M_\alpha \sqrt{\frac{K_B T_\alpha}{M_\alpha}}$.
The plasma plateau density is initially the same for ions and electrons, the value is set to $n_i = n_e = 2.0 n_{crit}$, where n_{crit} denotes the critical density defined in eq.(1.54).
The laser pulse has a linear polarization in the transverse direction, a peak amplitude of $a_0 = 2.0$ and duration of $60\,T$. The temporal profile has a $\sin^2$-like rising and falling ramp of one period length, and $58\,T$ of constant plateau.
As discussed in Par.(3.2.1), the process we are interested in is more efficient in case of a linearly polarized laser pulse because of the strong energy absorption and fast electron generation, in comparison with the case of circularly polarization where the electron heating is reduced. For this reason the laser pulse is linearly polarized in each simulation.
For reference, in all the following images the value of x is in units of laser wavelength λ, p_x is

in units of $m_e c$, the energy E in $m_e c^2$, the longitudinal electric field is in units of $E_0 = \frac{e}{m_e c \omega}$ and the density is relative to the critical value.

3.3.1 Cold ion simulation

First of all, we consider a simulation with a plasma of $10\,\lambda$ length, with initial temperature of $T_e = 5$ KeV , $T_i = 1$ eV that corresponds to a width of the distribution function in momentum space defined by $\sigma_e = 0.1\, m_e c$, $\sigma_i = 0.061\, m_e c$. The temporal and spatial resolution is set to $\Delta x = \Delta t = \frac{1}{1000}\lambda$. In the momentum grid the resolution is $\Delta p_{x,e} = 0.05\, m_e c$ and $\Delta p_{x,i} = 0.045\, m_e c$, respectively for electrons and ions.
The value of the ion temperature is chosen to be as close as possible to the zero temperature ($T_i = 0$) case, considering that the computational effort increases as the extension of the cell is reduced, since the number of mesh points must be raised.
The ion density is represented in Fig.(3.8), a first peak starts growing around $\simeq 12$ periods of interaction with the laser pulse, and it reaches the maximum value of $n_i \simeq 23\, n_{crit}$ as showed in the first frame. The propagation starts after $\sim 17\, T$ due to the radiation pressure effect. Since the hot electrons have been pushed back in the plasma but have not yet reached again the front surface, we regard the ion propagation as the first stage of the Hole Boring. Then a second peaked structure develops after $\simeq 22\, T$. We can observe that the distance between the two peaks increases during the propagation, because the velocity of the first one is greater than the other one. This difference suggests us that what we observe may be interpreted as a train of solitons rather than a coherent shock wave.

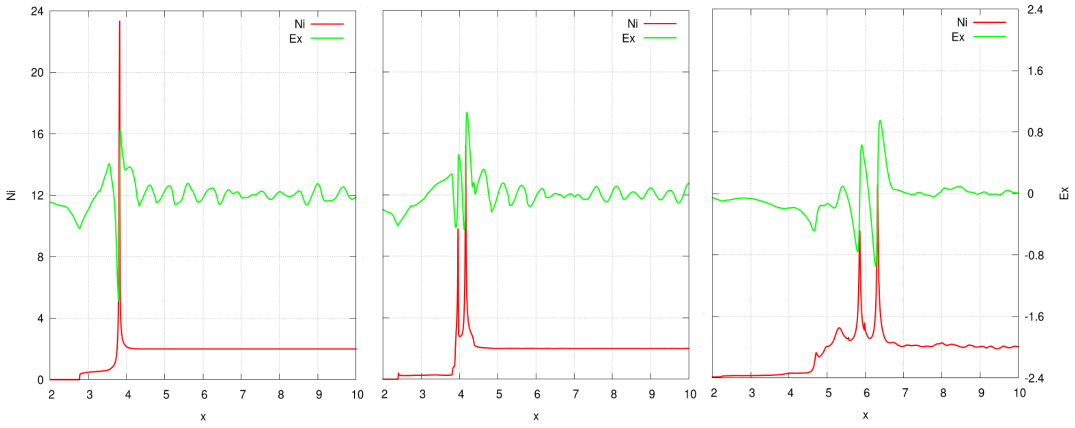

Figure 3.8: Ion density (red line) and longitudinal electric field (green line) at $t = 17, 27, 82T$.

Indeed, starting from eq.(3.7), where the constant K is fixed to the value mentioned in Par.(3.1), if we impose $\frac{\partial \phi}{\partial x} = 0$ we obtain a relation between the propagation velocity of the

soliton/shock and the maximum potential value ϕ_m, as

$$V_s = \sqrt{\frac{K_B T_e}{2M_i}} \frac{e^{\frac{e\phi_m}{K_B T_e}} - 1}{\sqrt{e^{\frac{e\phi_m}{K_B T_e}} - 1 - \frac{e\phi_m}{K_B T_e}}} \tag{3.26}$$

Thus, as observed in the simulation, the velocity increases with the amplitude of the electrostatic potential associated with the density peak.
For the sake of simplicity, in the following we refer to the first peaked structure as a shock.
In Fig.(3.9) we show the phase space of the ion distribution after 82 periods, and we evidence the portion of distribution function relative to the particles accelerated via the Hole Boring (HB) and the Collisionless Shock Acceleration (CSA).
We observe a fraction of particles that get trapped in the region between the two peaks which act as a potential well. In the phase space these particles are represented by the vortex structure behind the shock front.

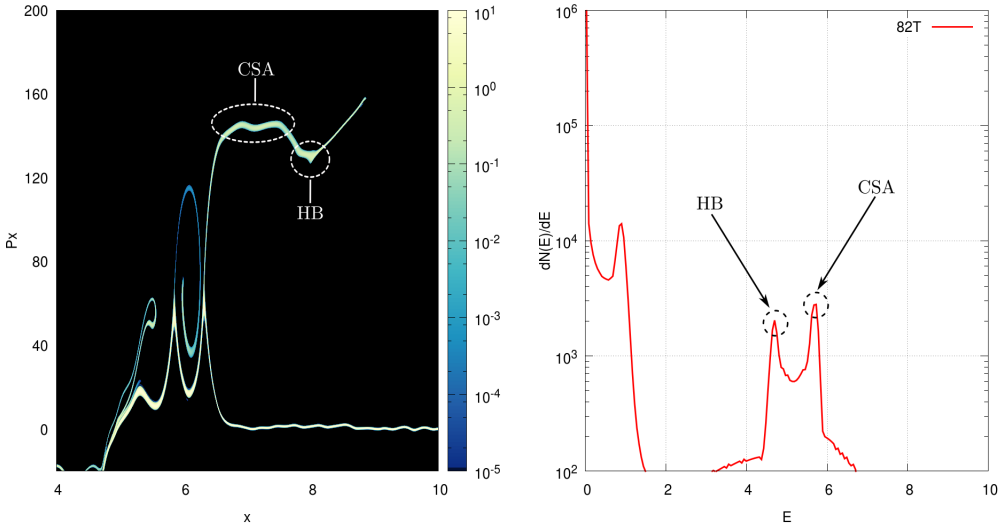

Figure 3.9: Left frame: Ion phase space at $t = 82\,T$. We point out the two mechanisms of acceleration observed, Hole Boring (HB) and Collisionless Shock Acceleration (CSA). The vortex structure represents the particles trapped behind the shock front. Right frame: Energy spectrum at $t = 82\,T$ in the x-range $6.3 \div 10\,\lambda$.

In the right frame of Fig.(3.9) we show the energy spectrum of the ion population in the range $x = 6.3 \div 10\,\lambda$, so that we take into account the particles in the shock front and all the accelerated ones.
The ion acceleration starts after $\simeq 25$ periods, when a first high energy ion bunch is generated by means of the Hole Boring mechanism, driven by the radiation pressure effect on the plasma

surface. The peak around $E \simeq 4.7\, m_e c^2$ arises in this first stage of the interaction and thus corresponds to the Hole Boring accelerated ions.
The plateau observed in the phase space relative to the ions reflected by the shock front, corresponds to the peaked structure with maximum at $E \simeq 5.7\, m_e c^2 \simeq 2.9\,\mathrm{MeV}$. There is a quite small energy spread $\frac{\Delta E_{\mathrm{HWHM}}}{E_{\mathrm{MAX}}} \sim 2\%$ corresponding to $\sim 0.06\,\mathrm{MeV}$.
From the simulation we can estimate the propagation velocity of the first density peak. In the time interval before $45\,T$ the velocity is $V_s \simeq 0.037\, c$ due to the piston action of the radiation pressure, then the shock starts propagating independently and the velocity acquires the stable value of $V_s \simeq 0.04\, c$ until $90\,T$. We can appreciate from Fig.(3.9) that the ions are accelerated by the shock front up to a momentum value $P \simeq 145\, m_e c$ that is in good agreement with twice the propagation momentum of the shock $P_s \simeq 72.6\, m_e c$.
Now we want to estimate the Mach number of the observed shock wave, defined as the ratio between the propagation velocity and the ion-acoustic speed $c_s \simeq \sqrt{\frac{\gamma_e T_e}{M_i}}$, where the polytropic index is $\gamma_e = 1$ in this case. To this aim we need to know the temperature of the electron population heated up during the interaction with the laser pulse.

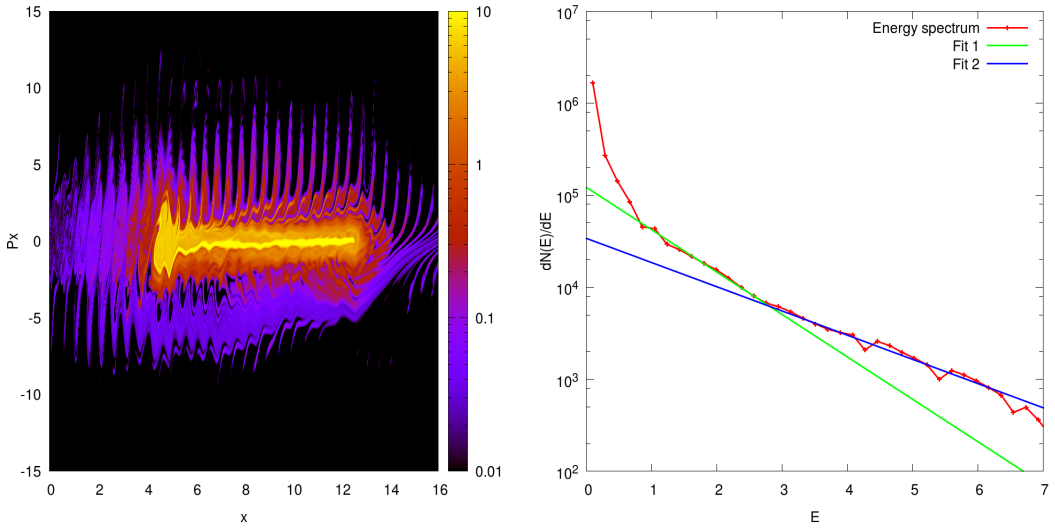

Figure 3.10: Left frame: Electron phase space at $t = 47\,T$. Right frame: Energy spectrum (red line) at the same time step, fitted function $\propto e^{-E/T_e}$. Fit 1 (green line) refers to the momentum interval $1.5 \lesssim \frac{p_x}{m_e c} \lesssim 3.5$, Fit 2 (blue line) refers to $\frac{p_x}{m_e c} \gtrsim 3.5$.

The temperature of the hot electrons can be estimated by the energy spectrum assuming that the electron distribution function is a Maxwellian distribution, so that $f(E) \propto e^{-E/T_e}$. Using logarithmic scale as in the right frame of Fig.(3.10) the slope of the linear fit is the inverse of the temperature. If more the one slope is clearly distinguishable, we speak about

different populations of particles and we assign their own temperature to each one. In our case, in the energy spectrum we observe that, besides the electrons that maintain the initial temperature, there are two characteristic temperatures for the hot electron population. The first population has momentum in the interval $1.5 \lesssim \frac{p_x}{m_e c} \lesssim 3.5$ (green line), the second one $\frac{p_x}{m_e c} \gtrsim 3.5$ (blue line). The fit reported in Fig.(3.10) give

$$T_{e,1} \simeq 0.48 \pm 0.03\,\mathrm{MeV} \quad ; \quad \mathrm{T_{e,2}} \simeq 0.84 \pm 0.04\,\mathrm{MeV} \tag{3.27}$$

It is by no means straightforward to understand in detail the energy distribution of the electrons heated by the laser pulse. We observe that the energy values go beyond what expected by the ponderomotive scaling.
Using the temperatures of (3.27) we estimate two values for the Mach number as

$$\mathcal{M}_1 = \frac{V_s}{c_{s,1}} \simeq 1.77 \quad ; \quad \mathcal{M}_2 = \frac{V_s}{c_{s,2}} \simeq 1.34 \tag{3.28}$$

where the subscript 1, 2 refer to the use of the temperature $T_{e,1}$ and $T_{e,2}$ respectively. Thus, using the highest temperature we obtain a value in the range expected by the theoretical model of Par.(3.1), while the other one slightly exceed the maximum value predicted, that is $\mathcal{M} = 1.6$. This value has been calculated within the assumption of Boltzmann equilibrium for the electron population, but in a more general case the existence of electrostatic shock with high Mach number has been predicted. In Ref.[37] allowing for electron trapping behind the shock front, the upper value is found to be $\mathcal{M} = 6.5$, above which only a pure piston solution can be found.
The population that is described by the highest temperature is the $\simeq 3.5\%$ of the total density in the upstream region and has kinetic energy greater than $\simeq 2.65\, m_e c^2$. On the other hand the fraction of electrons with kinetic energy $0.8 < E < 2.65$ in units of $m_e c^2$, is $\simeq 16\%$.
Once we know the value of the propagation velocity V_s and of the temperature of the electrons that drive the shock, we can graphically solve eq.(3.26) in order to estimate ϕ_m. Using as electron temperature $T_{e,2}$, derived by the electron energy spectrum at $t = 47\,T$, we obtain $e\phi_m \simeq 1.34 m_e c^2$, respectively with $T_{e,1}$ the value becomes $e\phi_m \simeq 1.44 m_e c^2$. These values are consistent with the one observed in the simulation, from which we obtain that the maximum potential, varies with time in a range

$$1.19 \lesssim \frac{e\phi_m}{m_e c^2} \lesssim 1.44 \tag{3.29}$$

A precise estimation of the maximum potential value is not straightforward, because of the hot electron bunches propagation that yields to a longitudinal electric field, and so to an

electrostatic potential non constant valued in the upstream region. Therefore in (3.29) we have calculated ϕ_m as the difference between the peak potential and the mean value of $\phi(x)$ in upstream region for each period.
Considering the potential barrier at $t = 47\,T$ as estimated for the highest temperature, the condition (3.24) is fulfilled by the particles with velocity and momentum in the laboratory frame

$$v_i > 1.7 \times 10^{-3}\, c \quad \rightarrow \quad P_i > 3.1\, m_e c \tag{3.30}$$

This value corresponds to ~ 50 times the characteristic width of the initial ion distribution. Therefore also the tails of the unperturbed Gaussian distribution are totally negligible in this region of the phase space. We should take into account that the condition (3.24) is quite sensitive to small variations of the maximum value of the electrostatic potential. Indeed, the highest value in the range (3.29) gives $P_i > 0.72\, m_e c$, required for the ion in order to get reflected. This momentum can be reached by a small fraction of particles, if we consider that the ion population in front of the shock is not unperturbed, but rather shows a turbulent behavior as we will discuss in Par.(3.3.3). Thus the fluctuation of ϕ_m and the turbulence of the ions in front of the shock may lead to a variable quantity of reflected ions with time, as showed in Fig.(3.11).

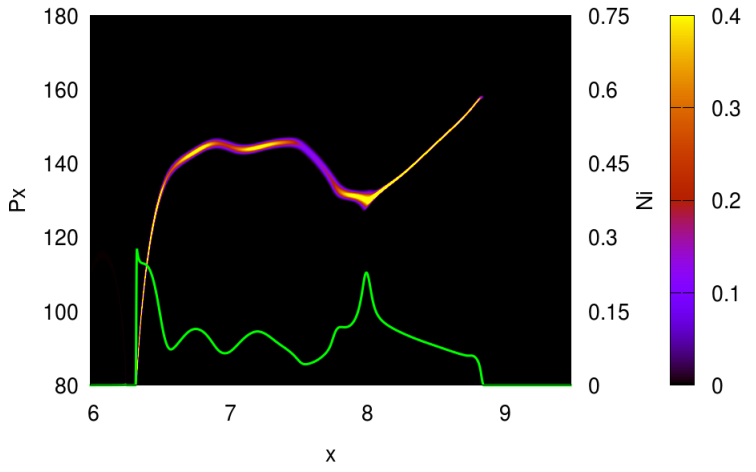

Figure 3.11: Portion of the ion phase space and density (green line) corresponding to the reflected ions at $t = 82\,T$.

We point out the variable amplitude of the distribution function value along the phase space plateau representing the reflected particles. Moreover we show the density of reflected particles (green line), calculated as first moment of the distribution function in the portion of the phase space reported in the figure. The density peak around $\sim 8\,\lambda$ may be attributed to the bunch of electrons accelerated via the Hole Boring mechanism and, as expected, the

peak value is greater than the density modulations relative to the electron bunches reflected by the shock front.
The simulation runs until 90 T, but till then we can not appreciate any damping in the shock front, and the resulting decreasing of the propagation velocity, since the condition $F(\phi_m) \ll 1$, mentioned in par.(3.2) is still fulfilled, the fraction of reflected ions remains smaller than 5 %.

3.3.2 Warm ion simulation

In order to study the effect of the initial ion distribution on the soliton or shock evolution, we perform a simulation with an initial warm ion population. Here, we report the results of a simulation carried out with the same parameters of the simulation with cold ions ($T_i = 1\,\text{eV}$) discussed in the previous paragraph (3.3.1), but with a wider initial ion distribution, defined by $\sigma_i = 1.37\, m_e c^2$ corresponding to a temperature $T_i = 500\,\text{eV}$.
In Fig.(3.12) we show a comparison between the ion density and the longitudinal electric field of this simulation and of the one initialized with cold ion population, reported in Par.(3.3.1). The ion density exhibits in both the simulations a double peaked structure, but with this initial condition (red line) the amplitude of each peak is reduced and the propagation velocity decreases. The same behavior is reproduced also by the longitudinal electric field (right frame).

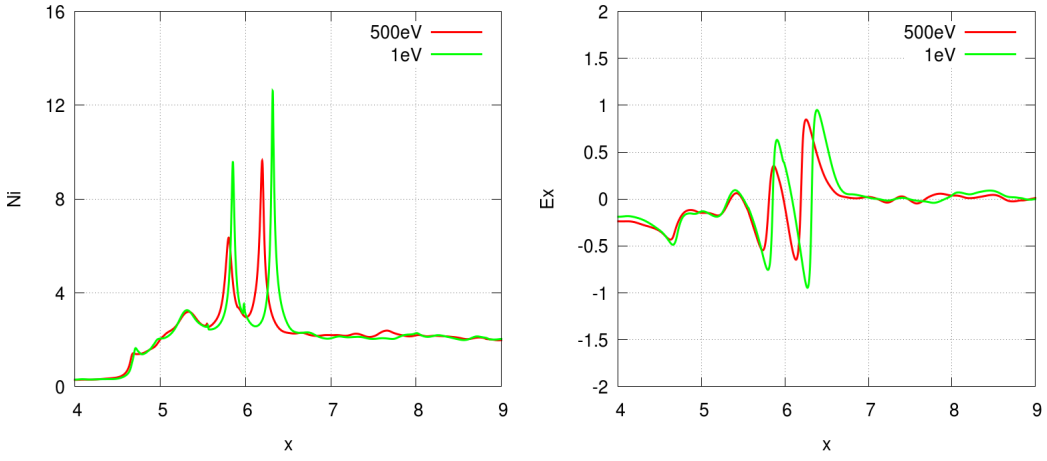

Figure 3.12: Left frame: Ion density. Right frame: Longitudinal electric field. Red line (respectively green line) represents the results of the simulation initialized with initial ion temperature $T_i = 500\,\text{eV}$ ($T_i = 1\,\text{eV}$) at $t = 85\,T$.

Since the laser pulse is the same for the two simulations, i.e. the same radiation pressure on

the plasma surface and the same electron heating effects, these differences can be associated with the greater number of particles that should be reflected in the warm plasma case with respect to the cold ion simulation. As in the case of cold ions, the second density peak propagates slower than the first one, and we observe the distance between the two peaks increasing with time.

In the first stage of interaction until $\sim 45\,T$, the velocity of the first peak is $V_s \simeq 0.035\,c$, then the shock detaches from the surface and starts propagating independently from the radiation pressure piston action gaining a velocity of $V_s \simeq 0.037\,c$. Therefore the expected momentum value for the reflected particles is $P \simeq 135.9\,m_e c$, that is represented by the plateau showed in the distribution function reported in Fig.(3.13).

The turbulence of the ion distribution function in the upstream region is still clearly visible, and we will analyze it in detail in the next paragraph (3.3.3). However, in this case the effect of the initial temperature, i.e. the broadening of the distribution function, is dominant since we observe a continuous and unmodulated reflection.

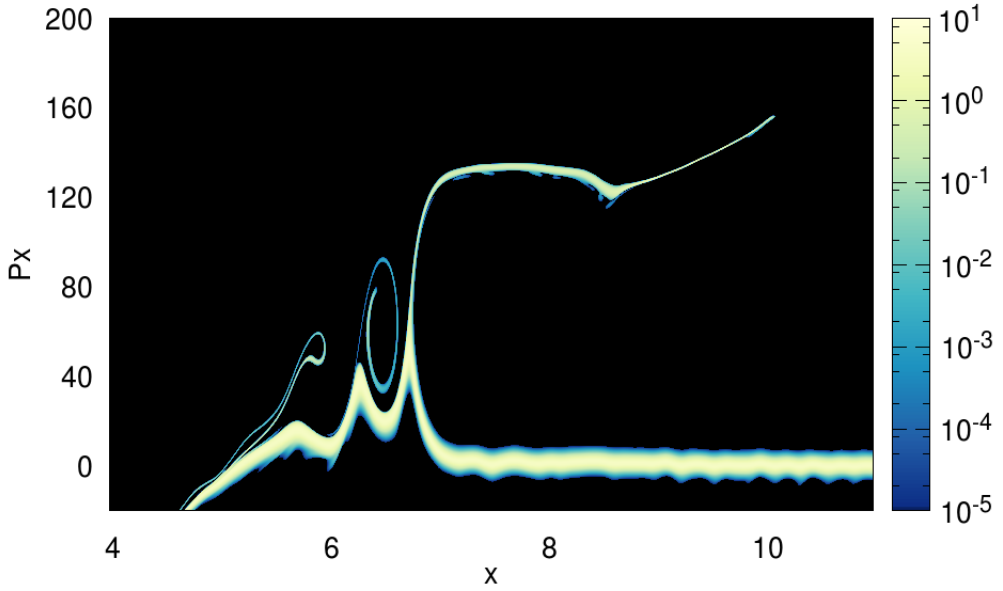

Figure 3.13: Ion phase space at $t = 97\,T$

In the time interval before $\sim 45\,T$ the radiation pressure acts as a piston and accelerates a bunch of ions. This fraction of accelerated particles has a relatively wide momentum and energy spread. In Fig.(3.14) the ion energy spectrum is showed at $t = 57\,T$ (red line), the ions already accelerated correspond to the broad structure around $\sim 4.2\,m_e c^2$ with a $\frac{\Delta E_{\mathrm{HWHM}}}{E_{\mathrm{MAX}}} \sim 7\%$ energy spread.

Then the monoenergetic peak at $\sim 4.9\,m_e c^2$ appears as results of the shock front reflection

and the number of particles that compose the peak increases with time, since the reflection in this case is almost continuous as showed in Fig.(3.13). The peak has a narrow energy spread $\frac{\Delta E_{\mathrm{HWHM}}}{E_{\mathrm{MAX}}} \sim 2\%$. The fraction of particles that get reflected, normalized to the unperturbed density in the same region, is $\simeq 5\%$ with respect to $\simeq 3\%$ of the previously analyzed case of cold ions population Par.(3.3.1).

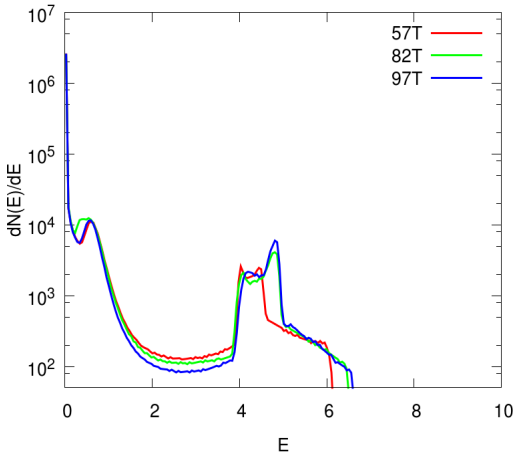

Figure 3.14: Ion energy spectrum for $t = 57\ ,\ 82\ ,\ 97\,T$, in a spatial region around the first density peak and including all the accelerated particles.

Thus, an initial warm plasma allows to obtain a monoenergetic peak with a small energy spread, composed by a greater number of reflected particles with respect to the case of initial cold ion. The disadvantage is that the energy peak value is reduced since the shock front propagates slower than with an initial cold ion population.

3.3.3 Ion density turbulence

We observe the growth of a perturbation in the ion density of the upstream region, where the shock has not yet passed, in the simulation initialized with both the ion temperature. Here we report the results of the simulation with plasma length $10\,\lambda$ and temperature $T_i = 1\,\mathrm{eV}$. As showed in Fig.(3.15), the density oscillations have a wavelength $\lambda_i \simeq \frac{\lambda}{4}$, where λ is the laser wavelength. The perturbation starts growing in the rear side of the plasma and checking the onset time, we find out that it corresponds to the interval in which the fast electrons, pushed back inside the plasma, have passed through this region.
The perturbation of the ion density affects the reflection from the shock front. As showed in Fig.(3.16), there is an oscillation in the distribution function of the ion corresponding to the density turbulence. The spatial fluctuation of the ion velocity may allows a fraction of ions to overpass the threshold value of eq.(3.24) so that they get reflected.

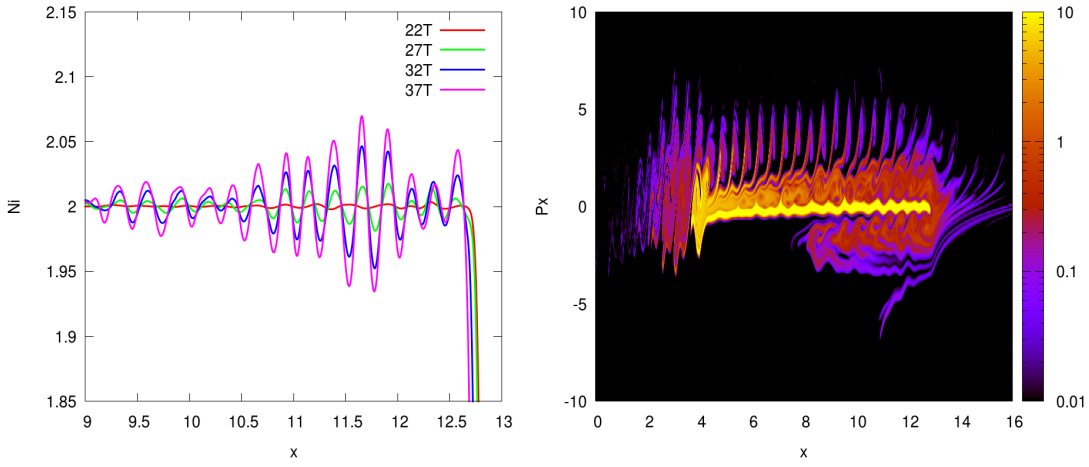

Figure 3.15: Left frame: Growing oscillations of the ion density that show the periodicity $\simeq \frac{\lambda}{4}$. Right frame: Electron phase space at $t = 22\,T$

We attribute the growing of this perturbation to the coupling of the ion density with the stream of the fast electrons, that propagate as bunches with periodicity 2ω and a velocity close to the speed of light, thus representing a perturbation of wavelength $\lambda_e \simeq \frac{\lambda}{2}$. The use of our Vlasov code makes more clear than the PIC simulations the observation of the main features of the turbulence, such as amplitude and periodicity. In the following paragraphs an analytic model will be presented and we will show the differences that arise with the two numerical approaches.

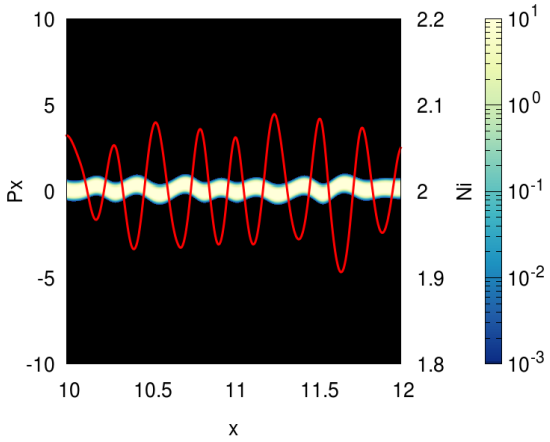

Figure 3.16: Portion of the ion phase space and ion density (red line), that show the oscillations at $t = 57\,T$.

3.3.4 Analytic model

Now we describe a simple model for the ion density oscillation with one quarter the wavelength of the laser pulse.
As initial condition, we assume an electron density described by three terms as

$$n_e = n_{0,e} + n_e^P + n_e^{NL} \tag{3.31}$$

where $n_{0,e}$ denotes the background electron density, n_e^P the hot electrons generated by the heating mechanism described in Par.(3.2.1), and n_e^{NL} a nonlinear perturbation.
The fraction of hot electrons, both the ones that propagate in the positive direction and the ones pushed back inside the plasma, are modeled as two external pump waves. These two waves are characterized by wavevector and frequency as (k^+, ω^+), (k^-, ω^-) that fulfill $k^\pm \simeq \frac{\omega^\pm}{c}$ since the electron bunches are fully relativistic. The two waves propagate in opposite direction, with generic relative phase. The physical quantities that describe the waves are

$$\begin{cases} n_e^P = \frac{1}{2}(n_e^+ e^{ik^+x - i\omega^+ t} + c.c.) + \frac{1}{2}(n_e^- e^{-ik^-x - i\omega^- t} + c.c.) \\ \\ v_e^P = \frac{1}{2}(v_e^+ e^{ik^+x - i\omega^+ t} + c.c.) + \frac{1}{2}(v_e^- e^{-ik^-x - i\omega^- t} + c.c.) \end{cases} \tag{3.32}$$

where we use the apex P to point out that we refer to the pump waves.
Since we are interested in the non linear terms deriving from the action of the pump waves, the system of fluid equations for the electron population can not be solved in the linear approximation. The non linear terms satisfy

$$\begin{cases} \partial_t n_e^{NL} + n_{0,e}\partial_x v_e^{NL} = -\partial_x(n_e^P v_e^P) \\ \partial_t v_e^{NL} = -v_e^P \cdot \partial_x v_e^P - \frac{eE^{NL}}{m_e} \\ \partial_x E^{NL} = -4\pi e n_e^{NL} \end{cases} \tag{3.33}$$

In detail, the solution we are seeking is an oscillation defined by $(\delta k, \delta\omega)$, with $\delta k = k^+ + k^-$ and $\delta\omega = \omega^+ - \omega^-$. In general, the non linear quantities of eq.(3.33) can be expressed as

$$n_e^{NL} = \tilde{n}_e e^{i\delta k x - i\delta\omega t} + c.c \tag{3.34}$$

similarly for the velocity and for the electric field. We can describe an oscillation as the one in Fig.(3.15), considering the case of $\omega^+ \simeq \omega^-$ and $k^+ \simeq k^-$, corresponding to an oscillation with frequency $\delta\omega \simeq 0$ and wavelength $\lambda_i = \frac{2\pi}{\delta k} \simeq \frac{\lambda_e}{2}$.
In the case in which the frequency exactly vanishes $\delta\omega = 0$, we look for the stationary solution imposing $\partial_t = 0$. Thus from the Poisson's equation we obtain a density perturbation with

amplitude $\tilde{n}_e = -\frac{m_e}{16\pi e^2}\delta k^2 v_e^+ v_e^{-^*}$.
For $\delta\omega \neq 0$, inserting eq.(3.32) in eq.(3.33), we obtain a relation for the amplitude of the non linear term of the electron density and for the electric field, both depending on the pump modes amplitude and phase

$$\tilde{n}_e = \frac{n_{0,e} v_e^+ v_e^{-^*} \delta k^2 + \delta k \delta\omega (n_e^+ v_e^{-^*} + n_e^{-^*} v_e^+)}{4(\delta\omega^2 - \omega_{p,e}^2)} \tag{3.35}$$

$$\tilde{E} = i\pi e \frac{n_{0,e} v_e^+ v_e^{-^*} \delta k + \delta\omega (n_e^+ v_e^{-^*} + n_e^{-^*} v_e^+)}{(\delta\omega^2 - \omega_{p,e}^2)} \tag{3.36}$$

The frequency that describes the observed oscillations is far from the resonance condition at the electron plasma frequency $\omega_{p,e}^2 = \frac{4\pi n_{0,e} e^2}{m_e}$ since $\delta\omega \ll \omega_{p,e}$.
Concerning the ion dynamics, the linearized fluid equations in the case of $T_i = 0$, are

$$\begin{cases} \partial_t n_i = -n_{i,0} \partial_x v_i \\ \partial_t v_i = +\frac{e(E^{NL} + E_{cd})}{M_i} \end{cases} \tag{3.37}$$

where $n_{i,0}$ denotes the unperturbed value of the initial density and E_{cd} is the electric field due to the charge displacement. Assuming quasi-neutrality of the plasma $n_i \simeq n_e$, which is justified if the perturbation wavelength is much greater than the Debye length, we obtain a relation

$$\frac{eE_{cd}}{M_i} \simeq -\frac{T_e}{M_i} \frac{\partial_x n_i}{n_{i,0}} \tag{3.38}$$

where the quantity $\sqrt{\frac{T_e}{M_i}}$ is the ion acoustic velocity c_s. Looking for a solution of the form $n_i = \tilde{n}_i e^{i\delta k x - i\delta\omega t} + c.c.$, and the same for the ion velocity, we obtain

$$\tilde{n}_i = i \frac{n_{0,i}}{M_i \delta k} \frac{e\tilde{E}}{(\frac{\delta\omega^2}{\delta k^2} - c_s^2)} \tag{3.39}$$

$$\tilde{v}_i = i \frac{\delta\omega}{M_i} \frac{e\tilde{E}}{(\frac{\delta\omega^2}{\delta k^2} - c_s^2)} \tag{3.40}$$

where a resonant condition is found when the ion oscillations acquire a wave phase velocity equal to the ion acoustic speed.
Eq.(3.40) in the case of $\delta\omega = 0$ shows that the ion velocity vanishes and no oscillations might be found. Now we report a simple calculation aimed at showing how a difference in the frequency of the incoming and reflected electron bunches may appear in our model. We take into account two consecutive bunches of hot electrons with a relative distance determined by the generation mechanism, in our case $\tau = \frac{\pi}{\omega}$ with ω the laser frequency, moving with velocity

$v \simeq c$ in the positive direction. When the first bunch reaches the rear side of the plasma, it can not escape because of the electrostatic confinement that acts as a wall reflecting all the particles. Since the back-holding electric field component that is generated by the charge separation drives an expansion of the plasma at the rear side, we should consider that the wall is moving with a velocity $u \ll v$, that can be estimated to be of the order of the ion acoustic velocity as in Ref.[38]. Thus, the velocity of the reflected bunches is shifted to the value $v' = v - 2u$.

Considering the first bunch reflected at the time $t_1 = 0$, the second one reaches the moving wall at a time instant $t_2 = \frac{v}{v-u}\tau$. Thus the distance between the two bunches propagating back inside the plasma is $\tau' = t_2 > \tau$. Regarding the bunches as a propagating waves as in the presented model, the waves are defined by the following parameters

$$\omega^+ = \frac{2\pi}{\tau} = 2\omega \tag{3.41}$$

$$\omega^- = \frac{2\pi}{\tau'} = \omega^+(1 - \frac{u}{v}) = 2\omega(1 - \frac{u}{v}) \tag{3.42}$$

where the apex + (respectively −) refers to the wave propagating in the positive (negative) direction. The wave vector for the reflected wave becomes

$$k^- = \frac{\omega^-}{v'} \simeq k^+(1 - \frac{u}{v})(1 + \frac{2u}{v}) \simeq k^+(1 + \frac{u}{v}) \tag{3.43}$$

Thus the frequency of the ion oscillations is $\delta\omega = \omega^+\frac{u}{v} \ll \omega^+$ and the wave vector is $\delta k \simeq 2k^+(1 + \frac{u}{2v})$. So we proved that the observed oscillation can be explained as a coupling of the ion response with the nonlinear term that describes an interaction between the two counterpropagating electron streams.

Until now we have considered the growing oscillation with $\delta k \simeq 2k$, by the same argument we obtain an oscillation with $\delta k = -2k$ with the same probability in case of completely symmetric initial condition for the electronic waves. With this assumption we would see a stationary oscillation that does not propagate, but considering a difference in the initial configuration, the ion perturbation may acquire a phase velocity.

3.3.5 Comparison with PIC code simulations

For each Vlasov simulation we make comparisons with PIC code simulations in order to verify if the results obtained with the PIC approach converge to the ones obtained with the Vlasov code. As we increase the number of particles per cell, we have a finer resolution of the phase space, thus a more accurate representation of the distribution function, and we expect the results of the two numerical approaches to show less differences.

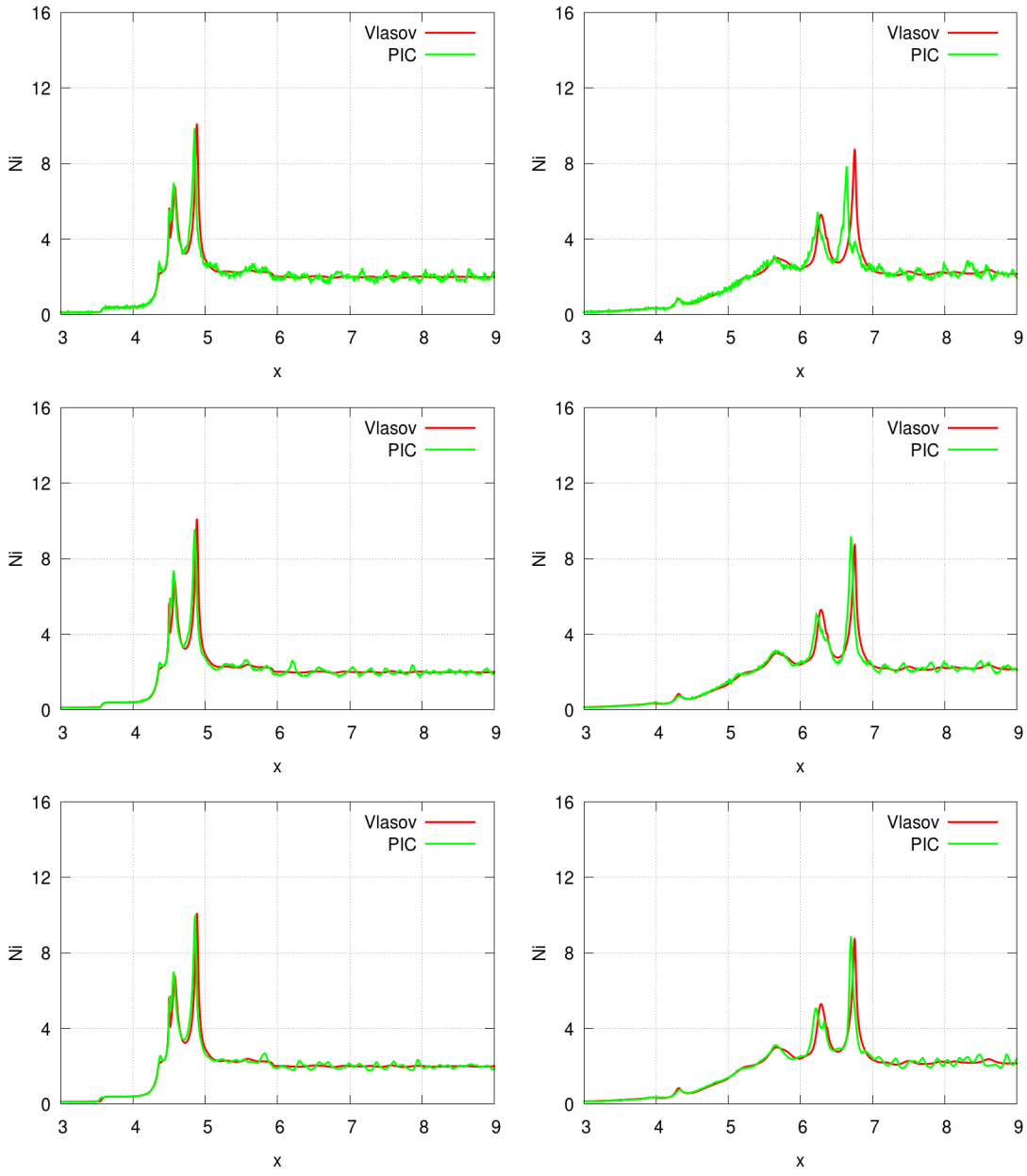

Figure 3.17: Ion density at $t = 47,\ 97\,T$ resulting from the Vlasov code (red line), and the PIC code (green line) using $N_p = 100$ (top frames), $N_p = 1000$ (central frames), $N_p = 10000$ (bottom frames).

The PIC simulations are carried out with resolution $\Delta x = \frac{1}{100}\lambda$, and all the other parameters are set as close as possible to the Vlasov code. We use a number of particles per cell $N_p = 100, 1000, 10000$. The increase of N_p of a factor 10 leads to a reduction of ~ 3 times the statistical noise, since it has a dependence $\propto \frac{1}{\sqrt{N_p}}$. Despite of the high number of particles used, the noise level prevents us from observing some details of the particles dynamics.
Both the simulations, with initial ion temperature $T_i = 1\,\text{eV}$ and $T_i = 500\,\text{eV}$ show a qualitatively good agreement with the PIC code results. The Vlasov code ion distribution function in the momentum space is not resolved with high precision in the case of low temperature, since a reduction of the extension of the cell $\Delta p_{x,i}$ entails an increase of the number of grid points, that lengthens the simulation time duration and increases the numerical effort. Because of that some differences may arise in the initial PIC and Vlasov configuration, due to this limited resolution. Here we present the comparison with the simulation initialized with warm ion population. As we observe from Fig.(3.17), both the ion density peaks propagate slower in the PIC than in the Vlasov simulation. As we increase the number of particles per cell, the distance between the peaks resulting from the two simulations is reduced. Moreover, the amplitude of the density peaks are very similar, with variation in the PIC code of the order of the fluctuations due to the numerical noise. Thus, with a higher number of particles per cell the simulation is more accurate and the main features are quantitatively in good agreement for the different numerical approaches. In more detail, we can observe in Fig.(3.17) that the ion density turbulence in front of the shock has a greater amplitude than in the Vlasov code, and this difference is still observable in the bottom frame of Fig.(3.17) although the noise is reduced.

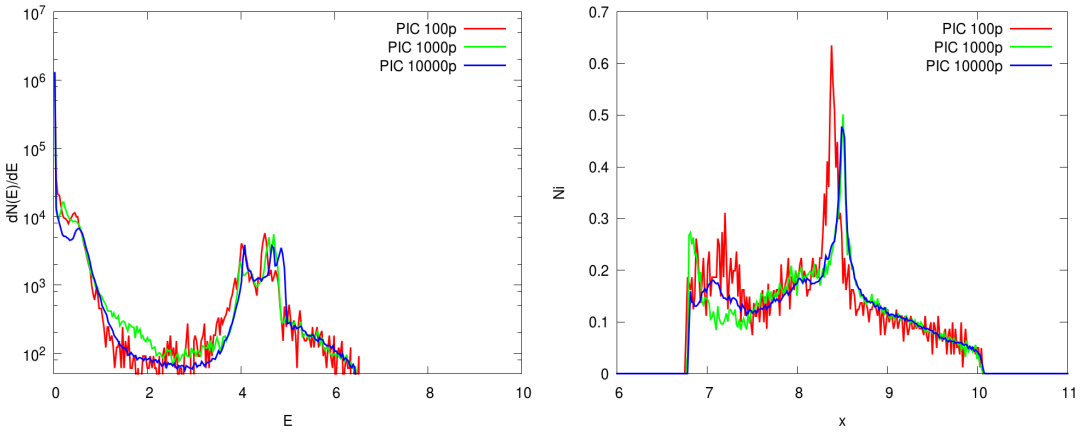

Figure 3.18: Ion energy spectrum and density of the accelerated particles at $t = 97\,T$ for the PIC simulations.

The difference between the propagation velocity can be associated with the energy that the shock gives to the accelerated particles. Indeed because of the effect of the turbulence the shock front loses an amount of energy slightly higher for the simulation with low number of particles per cell $N_p = 100$ with respect to the other tests. This can be inferred by Fig.(3.18) where we report the energy spectrum at $t = 97\,T$ for the three PIC simulations and the density of accelerated particles that have momentum $P > 100\,m_e c$, i.e. kinetic energy $E > 2.7\,m_e c^2$.
The left frame of Fig.(3.18) represents the same plot of Fig.(3.14). We can observe how the statistical noise prevent us a clear distinction of the peaked structures. However there is a good agreement between the results of the two numerical approaches.
Using a low number of particles per cell, some interesting details of the phase space can not be clearly identified. In Fig.(3.19) we show the electron phase space when the bunches of hot electrons have already recirculated in the target. We superimpose the macroparticles (red dots) of the distribution function resulting from the PIC simulation to the phase space of the Vlasov simulation. The structure in the most energetic tails of the distribution function can not be resolved by the PIC code.

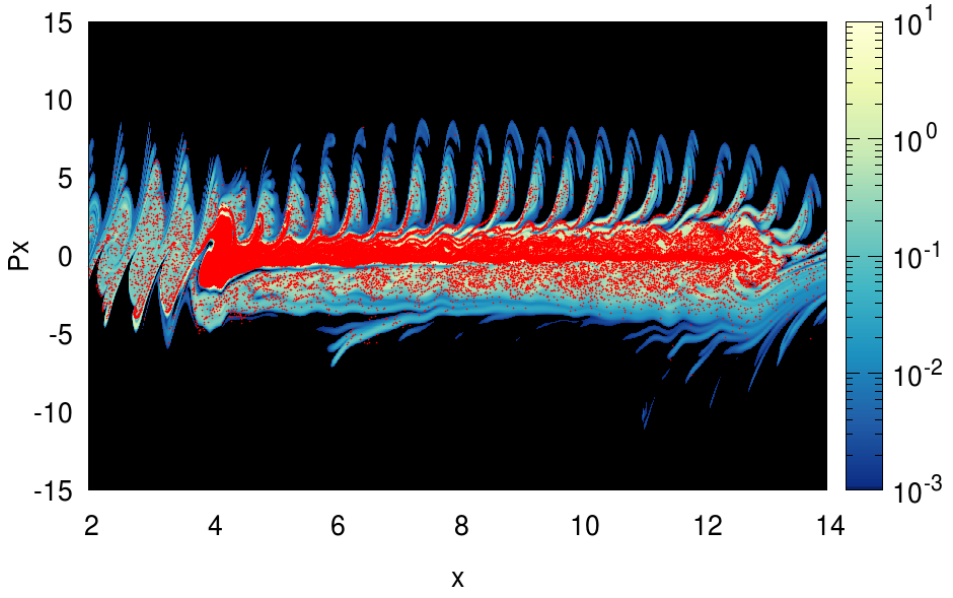

Figure 3.19: Electron phase space as result from the Vlasov and PIC (red dots) simulation at $t = 27\,T$.

Concerning the ion density perturbation, we show in Fig.(3.20) the three test simulations carried out with the PIC code. In the case of $N_p = 100$ the onset of the ion perturbation growth is covered by the statistical noise. At the later time the noise leads to a perturbation

with greater amplitude and we can not recognize the periodicity of $\simeq \frac{\lambda}{4}$. Increasing N_p the periodic structure is reproduced better but the amplitude is anyway much greater and noisy.

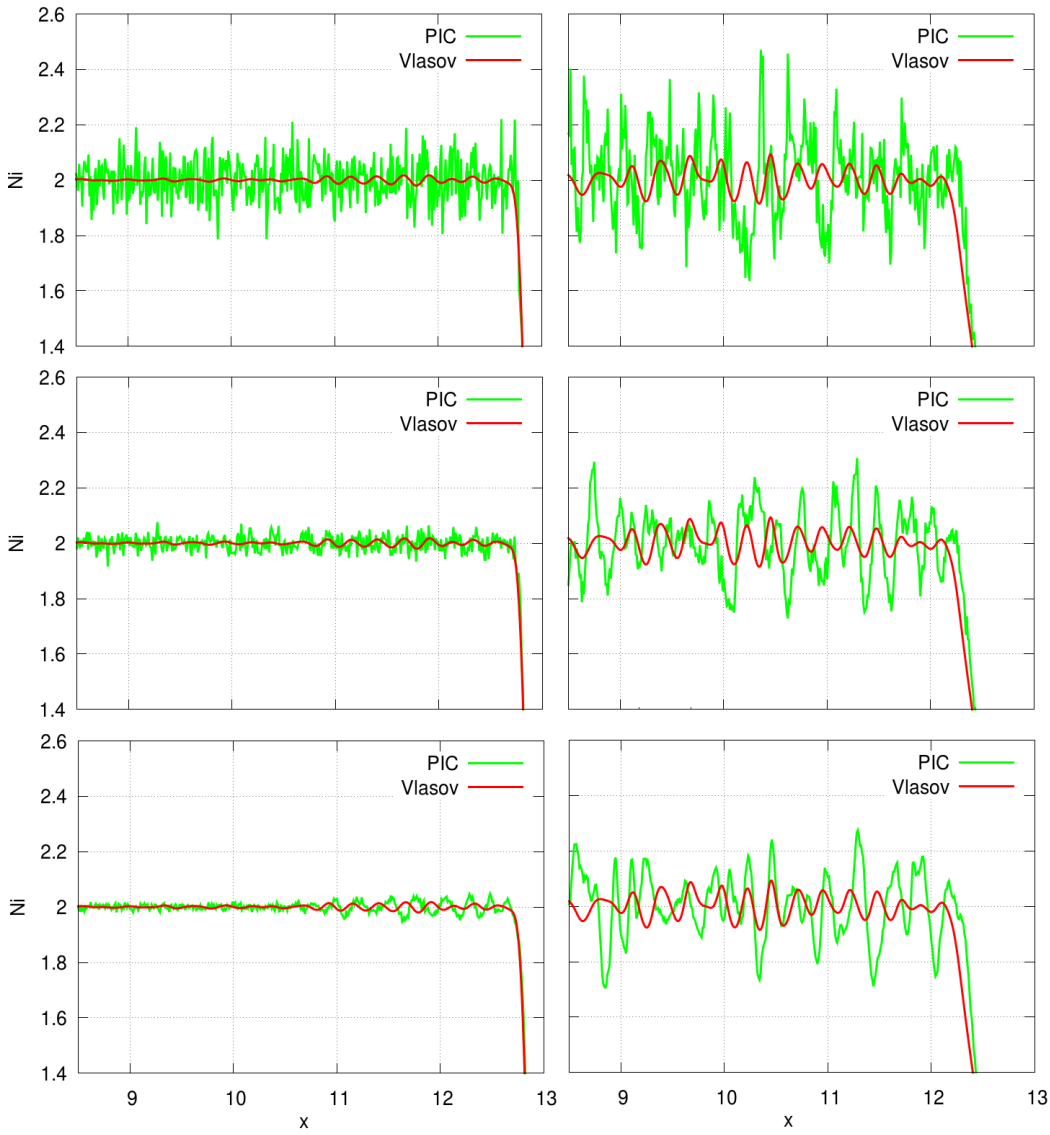

Figure 3.20: Ion density oscillation at $t = 27\,T$ (left frames) and $t = 77\,T$ (right frames). Comparison between the Vlasov code (red line) and PIC code (green line) with $N_p = 100$ (top frames), $N_p = 1000$ (central frames), $N_p = 10000$ (bottom frames).

The Fig.(3.21) shows how the above mentioned turbulence of the ion density, especially for the initial low temperature ion population, can not be neglected if we are interested in the study of accelerated particles energy spectrum. It is important to note that the increasing of the amplitude of the turbulence in the upstream region may affect the reflection, causing a different fraction of particles lying in a region of the phase space where condition (3.24) is not fulfilled.

Also the PIC code simulations reveal that the reflection is less continuous and stable for the cold ion distribution with respect to the warm ion case. For the cold ion simulation more quantitative differences caused by the turbulence are observed, such as the relative position of the two peaks respect to the Vlasov simulations, as showed in the left image of Fig.(3.21). In the warm ion case the thermal spread has an amplitude comparable with the turbulence, that therefore becomes less important for the acceleration process and there is a better agreement between the two numerical results as shown in the right frame.

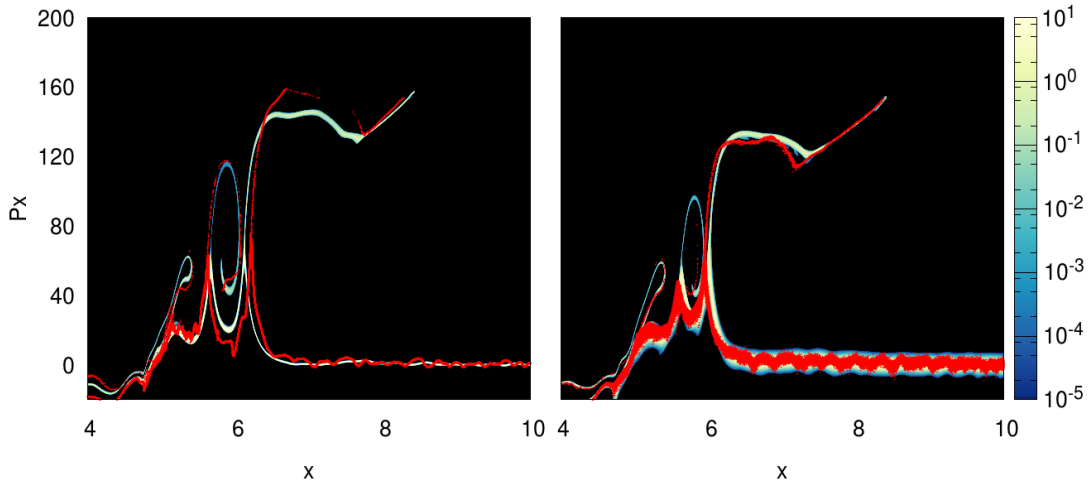

Figure 3.21: Ion distribution function at $t = 77T$ for the Vlasov and PIC (red dots) simulation with $N_p = 100$ for initial temperature $T_i = 1$ eV (left frame) and $T_i = 500$ eV (right frame)

Conclusions

In this thesis we have illustrated physical phenomena related to the nonlinear dynamics in laser-plasma interaction, mostly in the context of laser-plasma acceleration mechanisms. A numerical approach has been required due to the difficulties of the analytic description. An extensive numerical work has been carried out, starting with the development of a Vlasov code that allows for an accurate study of the phase space structures. For the integration of the Vlasov equation we have implemented the Time Spitting Scheme and the Positive and Flux Conservative Method. It was previously known that the TSS may cause a poor mass conservation in the relativistic electromagnetic regime, thus we have added a correction in order to allow for the study of a high intensity laser propagation and interaction with a plasma. All the results have been compared with PIC code simulations, in this way we have highlighted the main drawbacks of the PIC codes, such as high statistical noise level and lack of accuracy in the the study of low density regions of the phase space, while the Vlasov code provides a detailed representation of the distribution function in every regions of the phase space. Nevertheless the Vlasov approach involves a greater numerical effort with respect to the PIC simulations which run with the parameters generally used. Thus, a combined use of the two numerical approaches seems to be the best choice in order to exploit the main advantages of both the codes.

We have used the developed code for an in depth study of two mechanisms of particle acceleration, for electrons and ions respectively, in the frame of collisionless plasma interacting with an intense laser pulse. First, in the third chapter we have investigated on the wavebreak of a wake wave driven by a relativistically intense laser, propagating with phase velocity close to the speed of light in a thermal plasma and we have showed some novel features directly related to the relativistic particle kinematics.

The numerical integration of the fully relativistic 1D Vlasov equation with the developed Vlasov code, makes possible to study the self consistent evolution of the wake wave and the dynamics of the accelerated electrons, that reach values of their normalized momentum much larger than the wake wave phase momentum, i.e. well above the wavebreak threshold, which, in turn, is much larger than the thermal momentum. The detailed phase space representation

provided by the Eulerian integration of the Vlasov equation can be extended to the study, in the framework of an advanced particle acceleration scheme, of the plasma conditions and laser pulse parameters, needed to optimize the number and the spectrum of the electrons injected into the wake wave in a thermal plasma.
Most importantly the fraction of electrons, corresponding to the phase space spike that have reached the largest momentum, propagates for several tens of laser wave periods before being decelerated by the portion of the wake wave with a positive electric field. In addition, this spike in the momentum distribution produces an extremely steep density structure that propagates almost at the speed of light. Thus, our studies can be useful to clarify the conditions required to realize a relativistic flying mirror with a sufficiently large reflection coefficient in a thermal plasma. In this context we start preliminary tests that show a reflected pulse but further investigations will be carried out to characterize and improve its main features, such as frequency and amplitude.
In the second part we focus on the study of the interaction between an intense linearly polarized laser pulse and an overdense plasma, for the production of high energy ions by collisionless shock wave acceleration. We carried out simulations with different initial ion temperatures since we expect that the initial distribution function plays a key role in the ion acceleration dynamics.
We observe the generation of ion density multi-peaked structures whose propagation features depend on the laser pulse parameters. The structures start growing because of the action of the radiation pressure as a piston at the plasma surface, and a first bunch of accelerated ions is clearly observable in the energy spectrum. The energy value of this accelerated particles is in good agreement with the prediction of the Hole Boring mechanism. Then, as the electrons heated by the laser pulse recirculate inside the target, a shock wave which propagates with velocity greater than the hole boring one in launched. The acceleration of the background ions lying in the upstream region due to reflection from the shock front, leads to the appearance of a monoenergetic peak in the energy spectrum. As the initial ion temperature is increased the shock front propagates slower, so that the ions are accelerated at lower energy. Despite of that, with warm plasma the reflection appears to be more continuous and the number of accelerated ions is increased. The use of the Vlasov code allows the clear observation of an ion density oscillation, growing in the upstream region. We present a simple analytic model in which we associate the ions turbulence to the hot electrons propagating through the plasma. Within this model we can explain the main feature of the turbulence, that is the periodicity one quarter of the laser wavelength. We show that these oscillations may affect the reflection mechanism, since it may bring particles beyond the reflection threshold. Thus, the turbulence has an important role, above all in the simulation initialized with a cold ion population, in which case the theory predicts only the generation of a soliton wave. For this reason, in this simulation the observation of reflected ions should be associated with

the turbulence. Indeed, the fraction of particles that get reflected fluctuates with time, the reflection has less continuous nature although the energy peak in the spectrum maintains a small energy spread. Thus, our simulations suggest that it can be possible for given laser and plasma parameters, to find an optimal ion temperature as the best compromise between high energy ions and efficiency, that means monoenergetic beam and high number of accelerated particles.

Bibliography

[1] C. Villani. Particle systems and nonlinear Landau damping. Physics of Plasmas 21, 030901, 2014.

[2] C. K. Birdsall, A. B. Langdon. Plasma Physics via Computer Simulation. The Adam Hilger series on Plasma Physics, Bristol, Philadelphia and New York, 1991.

[3] C. Z. Cheng, G. Knorr. The Integration of the Vlasov Equation in Configuration Space. Journal of Computational Physics 22, pp. (330-351), 1976.

[4] E. Fijalkow. A numericalsolution to the Vlasov equation. Computer Physics Communications 116, pp. (319-328), 1999.

[5] E. Fijalkow. Numerical solution to the Vlasov equation: the 1D code. Computer Physics Communications 116, pp. (329-335), 1999.

[6] F. Filbet, E. Sonnendrucker, P. Bertrand. Conservative Numerical Schemes for the Vlasov Equation. Journal of Computational Physics 172, pp. (166-187), 2001.

[7] F.Huot, A. Ghizzo, P. Bertrand, E. Sonnendrucker, O. Couland. Instability of the time splitting scheme for the one-dimensional and relativistic Vlasov-Maxwell system. Journal of Computational Physics 185, pp. (512-531), 2003.

[8] N. V. Elkina, J. Buchner. A new conservative unsplit method for the solution of the Vlasov equation. Journal of Computational Physics 213, pp. (862-875), 2006.

[9] E. Hewitt, R. Hewitt. The Gibbs-Wilbraham phenomenon: An episode in Fourier analysis. Archive for History of Exact Sciences, 21, pp. (129-160), 1979.

[10] J. Büchner. Vlasov-code simulation. Proceedings of ISSS-7, 26-31 March, 2005.

[11] K. Nakajima et al. Observation of Ultrahigh Gradient Electron acceleration by Self-Modulated Intense Short Laser Pulse. Physical Review Letters 74, 4428, 1995.

[12] E. Esarey, C. B. Schroeder, W. P. Leemans. Physics of laser-driven plasma-based electron accelerators. Reviews of Modern Physics 81, 1229, 2009.

[13] T. Tajima, J. M. Dawson. Laser Electron Accelerator. Physical Review Letters 43, 267, 1979.

[14] R. Camassa, D. D. Holm. An Integrable Shallow Water Equation with Peaked Solitons. Physical Review Letters 71, 1661, 1993.

[15] P. Mulser, D. Bauer. High Power Laser-Matter Interaction. Springer, Berlin, 2010.

[16] A. I. Akhiezer, R.V. Polovin. Theory of Wave Motion of an Electron Plasma. Soviet Physics JETP 3, 696, 1956.

[17] J. Faure et al. Controlled injection and acceleration of electrons in plasma wakefields by colliding laser pulses. Nature 444, 737, 2006.

[18] A. Bergmann, P. Mulser. Breaking of resonantly excited electron plasma waves. Physical review E 47, 3585, 1993.

[19] S. V. Bulanov et al. On the breaking of a plasma wave in a thermal plasma: I. The structure of the density singularity. Physics of Plasmas, 19, 113102, 2012.

[20] S. V. Bulanov, T. Esirkepov, T. Tajima. Light Intensification towards the Schwinger Limit. Physical Review Letters 91, 085001, 2003.

[21] A. V. Panchenko et al. Interaction of electromagnetic waves with caustics in plasma flows. Physical Review E 78, 056402, 2008.

[22] S. V. Bulanov, F. Pegoraro, A. M. Pukhov. Two-Dimensional Regimes of Self-Focusing, Wake Field Generation, and Induced Focusing of a Short Intense Laser Pulse in an Underdense Plasma. Physical Review Letters 74, 710, 1995.

[23] M. Kando et al. Enhancement of Photon Number Reflected by the Relativistic Flying Mirror. Physical Review Letters, 103, 235003, 2009.

[24] S. V. Bulanov et al. On the breaking of a plasma wave in a thermal plasma: II. Electromagnetic wave interaction with the breaking plasma wave. Physics of Plasmas, 19, 113103, 2012.

[25] A. Stockem et al. Exploring the nature of collisionless shocks under laboratory conditions. Scientific Reports 4, 3934, 2014.

[26] A. Macchi, A. S. Nindrayog, F. Pegoraro. Solitary versus shock wave acceleration in laser-plasma interactions. Physical Review E 85, 046402, 2012.

[27] L. O. Silva et al. Proton Shock Acceleration in Laser-Plasma Interactions. Physical Review Letters 92, 015002 , 2004.

[28] M. Q. He et al. Acceleration dynamics of ions in shocks and solitary waves driven by intense laser pulses. Physical Review E 76, 035402, 2007.

[29] D. Haberberger et al. Collisionless shocks in laser-produced plasma generate monoenergetic high-energy proton beams. Nature Physics 8, pp.(95-99), 2012.

[30] C. A. J. Palmer et al. Monoenergetic Proton Beams Accelerated by a Radiation Pressure Driven Shock. Physical Review Letters 106, 014801, 2011.

[31] A. Macchi, T. V. Liseikina, S. Tuveri, S. Veghini. Theory and simulation of ion acceleration with circularly polarized laser pulses. C. R. Physique 10, 207, 2009.

[32] D. A. Tidman, N. A. Krall. Shock waves in collisionless plasmas. Wiley-Interscience, New York, 1971.

[33] F. Brunel. Not-so-resonant, resonant absorption. Physical Review Letters 59, 52, 1987.

[34] A. Macchi, M. Borghesi, M. Passoni. Ion acceleration by superintense laser-plasma interaction. Review of Modern Physics 85, 751, 2013.

[35] H. Popescu et al. Subfemtosecond, coherent, relativistic, and ballistic electron bunches generated at ω_0 and $2\omega_0$ in high intensity laser-matter interaction. Physics of Plasmas 12, 063106, 2005.

[36] A. Macchi, F. Cattani, T. V. Liseikina, F. Cornolti. Laser Acceleration of Ion Bunches at the Front Surface of Overdense Plasmas. Physical Review Letters 94, 165003, 2005.

[37] D. W. Forslund, J. P. Freidberg. Theory of Laminar Collisionless Shocks. Physical Review Letters 27, 1189, 1971.

[38] P. Mora. Plasma Expansion into a Vacuum. Physical Review Letters 90, 185002, 2003.